EFFECT OF ORGANIC LUMINESCENCE MATERIALS ON CARBON-BASED PEROVSKITE SOLAR CELL EFFICIENCY

TEJAS SHARMA

MASTER OF ENGINEERING SCIENCE

LEE KONG CHIAN FACULTY OF ENGINEERING AND SCIENCE

UNIVERSITI TUNKU ABDUL RAHMAN

JULY 2024

Effect of Organic Luminescence Materials on Carbon-Based Perovskite Solar Cell Efficiency

By

TEJAS SHARMA

A dissertation submitted to the

Department of Mechanical and Material Engineering,

Lee Kong Chian Faculty of Engineering and Science,

Universiti Tunku Abdul Rahman,

in partial fulfilment of the requirements for the degree of

Master of Engineering Science

July 2024

ABSTRACT

EFFECT OF ORGANIC LUMINESCENCE MATERIALS CARBON-BASED PEROVSKITE SOLAR CELL EFFICIENCY

Tejas Sharma

Integrating organic long persistent luminescence (OLPL) materials into carbon-based hole-transport free perovskite solar cells (C-PSCs) offers a favorable route to improving the performance and efficiency of next-generation photovoltaic cells. The majority of luminous materials in the market today are derived from an inorganic compound that needs extremely high processing temperatures and rare elements like dysprosium and europium. These materials are known as inorganic long-persistent luminescence (ILPL) materials. In the same way, OLPL materials, which are also known for their capacity to continue emitting light even after excitation stops, have special benefits for extending solar harvesting and optimizing energy conversion processes. PSCs have advanced significantly in the last few years, but there are still certain problems that prevent PSCs from being commercialized such as sensitivity to heat, light, and moisture, which cause instability and eventually reduce their performance. C-PSCs use carbon materials that can function as hole-transport layers (HTL) as well as extraction layers, helping to lower HTL not only lower production costs and improve the device's stability.

The goal of this work was to develop LPL-based C-PSC by employing carbon paste as a counter electrode. Furthermore, in this work, the use of blended OLPL materials of N,N,N′, N′-tetramethylbenzidine (TMB), and 2,8- bis (diphenylphosphoryl) dibenzo [b,d] thiophene (PPT) in PSCs was also investigated. Using the melt-casting process, several samples with various ratios of TMB and PPT were prepared. PSCs were prepared where the compact and mesoporous solutions of the electron transport layer (ETL) were deposited on FTO substrate. Then light absorber layer of perovskite was applied over the ETL layer, followed by carbon electrode layer. A simple approach was adopted in which an active layer of LPL material was externally coupled to the C-PSCs, achieving the champion efficiency of 7.65% with ILPL at ambient conditions. Besides optimizing the PSCs device, the emission decay rate, overall performance, and the dynamics of charge kinetics were studied. Among the various samples of LPL, cell-3 (TMB: PPT 7:3) has the longest lifetime and the highest photon counts, suggesting the lower rate of electron decay. A successful evaluation was conducted on the all-day C-PSC with organic and ILPL materials. The C-PSC device was tested upto 1680 hours. Unfortunately, coupling the PSC sample with the OLPL layer did not exhibit positive effects. However, the results demonstrate that PSCs can be fabricated under ambient conditions, although further improvement is required in the configuration of PSC with LPL.

Keywords: Perovskite Solar cells, Organic luminescence materials, photoluminescence, power conversion efficiency,

ACKNOWLEDGMENT

Firstly, I would like to sincerely thank my Supervisor Ts. Dr. Jun Hieng Kiat, and co-supervisor Dr. Ng Chai Yan for their guidance and strong expertise in photovoltaic fields. Their support throughout my master's program has motivated me to continue exploring this field of study. From designing experiments to analyzing results and writing a research paper for peer review, I've gained invaluable insights through their patient mentorship. These past two years have been the most productive of my life, largely thanks to their guidance and expertise.

I am grateful to the Lee Kong Chian Faculty of Engineering and Science, Universiti Tunku Abdul Rahman for providing me with the opportunity and platform to push my limits with this project. Additionally, I want to express my sincere appreciation to all the laboratory staff and technicians who have supported me with their invaluable assistance throughout my research journey. I am thankful to my senior Mr. Yew Hang Soo, who has been helping me since I began working in the lab.

I would like to express my gratitude towards Prof. Pramod K. Singh, from Sharda University, (India) for his constant encouragement, and invaluable guidance which encouraged me a lot to pursue research.

APPROVAL SHEET

This thesis/dissertation entitled **"EFFECT OF ORGANIC CARBON-BASED PEROVSKITE SOLAR CELLS EFFICIENCY"** was prepared by Tejas Sharma and submitted as partial fulfillment of the requirements for the degree of Master of Engineering Science at Universiti Tunku Abdul Rahman.

Approved by:

_____jun hk_____

(Ts. Dr Jun Hieng Kiat)

Associate Professor/Supervisor   Date: 09 July 2024

Department of Mechanical and Material Engineering

Lee Kong Chian Faculty of Engineering and Science

Universiti Tunku Abdul Rahman

_chaiy_____

(Dr. Ng Chai Yan)

Assistant Professor/Co-supervisor   Date: 09 July 2024

Department of Mechanical and Material Engineering

Lee Kong Chian Faculty of Engineering and Science

Universiti Tunku Abdul Rahman

LEE KONG CHIAN FACULTY OF ENGINEERING AND SCIENCE UNIVERSITI TUNKU ABDUL RAHMAN

Date: 09/07/2024

SUBMISSION OF THESIS DISSERTATION

It is hereby certified that **Tejas Sharma** (ID No: 22UEM00754) has completed this thesis/dissertation entitled **"EFFECT OF ORGANIC LUMINESCENCE MATERIALS CARBON-BASED PEROVSKITE SOLAR CELLS EFFICIENCY"** under the supervision of Ts. Dr. Jun Hieng Kiat (Supervisor) from the Department of Mechanical and Material Engineering, Lee Kong Chian Faculty of Engineering and Science, and Dr. Ng Chai Yan (Co-Supervisor) from the Department of Mechanical and Material Engineering, Lee Kong Chian Faculty of Engineering and Science.

I understand that the University will upload softcopy of my dissertation in pdf format into UTAR Institutional Repository, which may be made accessible to UTAR community and public.

Your truly

(Tejas Sharma)

Tejas Sharma

x

DECLARATION

I **Tejas Sharma** hereby declare that the thesis/dissertation is based on my original work except for quotations and citations which have been duly acknowledged. I also declare that it has not been previously or concurrently submitted for any other degree at UTAR or other institutions.

<div align="right">

(Tejas Sharma)

Tejas Sharma

Date: 09/07/2024

</div>

TABLE OF CONTENT

LIST OF TABLES

LIST OF FIGURES

LIST OF ABBREVIATIONS

C-PSC	Carbon-based perovskite solar cell
C-TiO$_2$	Compact-titanium dioxide
DMF	Dimethylformamide
DMSO	Dimethyl sulfoxide
ETL	Electron transport layer
EIS	Electrochemical impedance spectroscopy
FTO	Fluorine-doped tin oxide
FAMAPbI3	Formamidinium methylammonium lead iodide
FESEM	Field-emission scanning electron microscope
FF	Fill factor
HTL	Hole transport layer
HTL-free PSC	Hole transport layer-free perovskite solar cell
HRTEM	High-resolution transmission electron microscopy
ILPL	Inorganic long persistent luminescence
J$_{sc}$	Short-circuit current density
LPL	Long-persistent luminescence
MAPbI$_3$	Methylammonium lead Iodide
m-TiO$_2$	Mesoporous titanium (IV) oxide
OLPL	Organic long persistent luminescence
PSC	Perovskite solar cell
PSCs	Perovskite solar cells
PPT	2,8-Bis(diphenyl-phosphoryl) dibenzo[b,d]thiophene
PCE	Power conversation efficiency
PL	Photoluminescence
Rs	Series resistance

SEM	Scanning electron microscope
SCs	Solar cells
Sec	Seconds
TMB	3,3′,5,5′-Tetramethylbenzidine
TRPL	Time-resolved photoluminescence
UV-Vis	Ultraviolet-visible light spectroscopy
V_{oc}	Open-circuit voltage
XRD	X-ray diffraction

CHAPTER-1

INTRODUCTION

1.1 General Introduction

The world now relies on exhaustible fossil fuels to provide around 85% of its energy needs, which impacts both the environment and human health. Moreover, by 2050, it is expected that the world's energy consumption will have doubled (Nazeeruddin, 2016). Several factors contribute to this increase, including population growth, economic development, urbanization and rises in energy needs in emerging economies (Osobajo et al., 2020). As a result, it becomes urgently necessary to boost renewable energy sources including solar, wind, and water energy. In recent years, the world has been paying more and more attention to solar energy because of its abundance, affordability, and environmentally friendly nature; this has led to the fast advancement of solar cells (SCs). Based on the materials and technology, SCs are categorized into three different generations in which a wide range of SCs including silicon-SCs, thin film SCs, cadmium telluride (CdTe-SCs), organic SCs, dye-sensitized solar cells (DSSCs), and PSCs have been developed. Third-generation SCs have power conversion efficiencies (PCE) that are comparable to those of conventional silicon-based SCs but they also have less weight, more flexibility, and lower manufacturing costs. However, it faces challenges related to stability and long-term durability which

limits their applications (Tang et al., 2017 ; J.D. et al., 2022). Therefore, researchers are searching for novel, inexpensive, and environmentally friendly light-absorbing materials for SCs, and a new class of third-generation SCs named PSCs was developed which provides an alternative to silicon solar cells.

In 1839, Gustav Rose found the first perovskite, he discovered the perovskite compound of calcium titanate ($CaTiO_3$), which has a three-dimensional octahedral crystal structure. Due to its adaptability, the perovskite structure has found extensive use in numerous applications, which includes batteries, fuel cells and more recently, photovoltaics. Later, the term "perovskite" is widely used to refer to compounds having the structure ABX_3, where A is an organic or inorganic group, B is a metal and X is a non-metal, typically oxygen and halogen. Over the past decade, PSCs have seen remarkable progress with efficiencies increasing from 3.8% to 28.1%. With their remarkable improvements in efficiency and cost-effectiveness, currently, PSCs are one of the most promising renewable energy technologies (Snaith, 2013 ; Yang et al.,2017). The remarkable optoelectronic features of halide PSCs including their ambipolar carrier diffusion capabilities, variable bandgap, long carrier diffusion length, and excellent polycrystalline mineralization at low temperatures, have attracted a lot of research attention. Because of all these benefits, PSCs have achieved the PCE of 28.1% (Liu et al., 2023) Despite having a high efficiency of solar-to-electric conversion, PSCs still have issues such as sensitive to moisture, light, and heat which results in lower performance and instability due to expose in certain environmental conditions

throughout fabrication and storage procedures (Azmi et al.,2018). Generally, there are 5 main components in PSCs: a perovskite light-absorbing layer, an electron transporting layer (ETL), a hole transporting layer (HTL), cathode electrodes, and anode electrodes as shown in Figure 1.1. The bottom electrode is usually coated with conductive oxide either indium tin oxide (ITO) or fluorine-doped tin oxide (FTO). The ETL is a metal oxide semiconductor made of zinc oxide (ZnO) titanium dioxide (TiO$_2$), or tin dioxide (SnO$_2$) (Azmi et al., 2018 ; Chen et al.,2018). Poly[bis(4- phenyl)(2,4,6-trimethylphenyl)amine] (PTAA), copper thiocyanate (CuSCN), 2,2′,7,7′-Tetrakis[N,N-di(4-methoxyphenyl)amino]-9,9'- spirobifluorene (spiro- OMeTAD) are frequent HTL materials. For the top electrode, metallic electrodes made of gold (Au), silver (Ag), and aluminum (Al) are being employed using thermal evaporation or hot-pressing methods (Assi et al., 2021; Zhao et al., 2019).
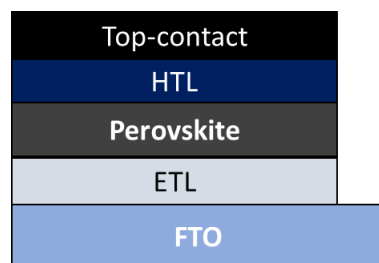
Figure 1.1 Components of PSC

Methylammonium lead iodide (MAI), which is well-known for having good optoelectronic properties, is the most investigated perovskite material that is frequently studied in the field of SC research where methylammonium (MA) serves

as the organic cation. The direct bandgap, intense light absorption, and extended carrier diffusion lengths are the main optical and electrical properties of MAI perovskite. Because of these properties, it is perfectly suited for solar applications. The perovskite films of MAI can be created by spin coating and inkjet printing which provide affordable and scalable manufacturing procedures. Moreover, the band gap of perovskite can be tuned by changing the concentration of halogen element present in the perovskite structure (Lee et al., 2018). Additionally, MAI perovskite can be used in tandem SC design, where many layers of various materials are stacked to improve the overall PCE. The development of extremely effective tandem or tandem-PSCs is made possible by the compatibility of MAI perovskite with other photovoltaic materials (Bett et al., 2020). Despite that, there are several difficulties linked with $MAPbI_3$-based PSCs, mainly regarding their enduring stability and durability. The primary cause of PSC instability is the degradation of both the electrode materials and the perovskite semiconductor, and the interfaces. Researchers have explored alternative materials, such as formamidinium lead iodide $FAPbI_3$, has a longer charge diffusion length and a lower band gap at room temperature (Qiao et al., 2022 ; Salim et al., 2021). Several studies have suggested partially substituting smaller MA or Cs cations for bigger FA cations in $FAPbI_3$ to stabilize the perovskite phase (Quanyao et al.,2023; Dehingia et al., 2022 ; Yi et al., 2016).

An alternative strategy to improve the functionality or performance of PSCs in certain aspects is to incorporate long persistent luminescence (LPL) materials in SCs. After being subjected to light, a material may exhibit the light for an extended period of time, this

phenomenon is known as long persistent luminescence. LPL phenomenon is exhibited by certain materials in which they can emit light for an extended period after being exposed to light or other forms of energy (Li et al., 2016). There are two main types of LPL materials: OLPL and ILPL. OLPL materials are typically composed of conjugated polymers, which are long chains of molecules containing alternating single and double bonds. When these polymers are excited by light, they emit light as the electrons in the double bonds relax back to their ground state (Alam et al., 2022). On the other hand, ILPL materials, consist of transition metal complexes, which are molecules containing a transition metal ion surrounded by ligands. When these complexes are excited by light, the electrons in the transition metal ion relax back to their ground state, resulting in light emission (Vaidyanathan, 2023). LPL materials have numerous applications including displays, surveillance and security, medical diagnostics, sensors, and photovoltaic cells (Kumar Soni & Pratap Singh, 2020 ; Eeckhout et al., 2010 ; Liu et al., 2021). In addition to their unique ability to emit long-lasting light after excitation and their lattice structure that slowly releases trapped energy, LPL materials could enhance SC performance under low light conditions. Nowadays, optical research makes considerable use of ILPL materials based on strontium aluminum oxide ($SrAl_2O_3$) doped with Eu, Dy (Matsuzawa et al., 1996).

In this study, the effects of OLPL namely 3,3′,5,5′- Tetramethylbenzidine (TMB) and 2,8-Bis(diphenyl-phosphoryl) dibenzo[b,d] thiophene (PPT), on PSCs were investigated using two different approaches for LPL integration. The first method connects LPL externally through a tiny glass substrate, while the second modifies the ETL to include LPL. A one-step spin-coating approach employing the vacuum-assisted solution procedure (VASP) was used to deposit the perovskite films lacking an HTL-free material in their structure. This configuration is known as HTL-free PSCs (X. Li et al., 2016).

1.2   Problem Statement

Research on PSC has shown tremendous potential and development for the advancement of renewable energy technology. However, there are still certain problems that prevent PSCs from being commercialized i.e. the interaction of perovskite is unstable when exposed to moisture, oxygen, and changes in temperature throughout the manufacturing. Additionally, the significant energy consumption associated with the fabrication of charge-transport layer (such as P3HT, PTAA and spiro-OMeTAD) and noble metal counter electrodes (i.e., Ag and Au). The manufacturing procedures for these CTL and electrodes deposition makes them unfavorable for wide-scale production (Pradid et al., 2021; Babu et al.,2020). Humidity is one of the main causes of the degradation of perovskites, and this is due to the hygroscopic nature of amine, which presents in MAPbI3. Therefore, various methods have been approached to overcome the stability. The strategies involve modifying the perovskite lattice structure to enhance its resistance to moisture. Another approach is doping in the charge-transporting layers (HTL & ETL), and passivation by using various materials (polymers, quantum dots) (Duan et al., 2019). Also, alternative materials can be employed as counter electrodes in PSCs to overcome these problems, including Al, Cu, ITO, PEDOT: PSS, carbon, and carbon derivatives (Y. Xu et al., 2022). Carbon-based materials have several advantages because of their remarkable thermal and electrical conductivity, electrochemical stability, water resistance, and hydrophobic nature. They possess a

work function of 5.0 eV, similar to Au (5.1 eV) and Ag (4.6eV) (Y. Xu et al., 2022). To address the material cost issue, this study was planned to develop hole transport material-free PSC using carbon paste as a counter electrode. Furthermore, the integration of LPL in PSC was studied.

Alternatively, LPL materials present in the market are based on the inorganic system of strontium aluminum oxide ($SrAl_2O_4$) doped with europium and dysprosium and emit for more than ten hours. However, the fabrication of this system necessitates the use of rare elements and temperatures above 1,000°C (P. Li et al., 2022). Additionally, OLPL has not been studied extensively in which the optical characteristics have not been investigated thoroughly, although they possess the same properties as inorganic LPL. An LPL material has several advantages for SCs. LPL can store energy and release it slowly when exposed to light as luminescence over time. By using this characteristic, effective sunlight harvesting duration may be extended beyond the hours of daylight (Chiatti et al., 2021). To provide a constant power source, the stored energy can be progressively released at night or in low light. Conventional perovskite materials would not be able to effectively employ diffuse or low-intensity sunlight, whereas persistent luminescence materials can capture and store the sunlight. Moreover, the exceptional chemical and thermal stability of some LPL materials can enhance the stability of PSCs (Saliba et al., 2016 ; L. Zhang et al., 2022). Therefore, this work demonstrates the novel approach to increase the light conversion of PSCs with the employment of blended OLPL materials. Furthermore, the synergistic effect of LPL and light can improve the photoelectric outcome of SCs containing

LPL by manipulating the energy gap between charge- transfer and excited states of the materials. This may help to extend light absorption and charge generation by resolving the narrow absorption range as a result enhancement in devices overall efficiency.

1.3 Aim & Objective

This study aims to optimize the blended organic long persistent luminescence (LPL) materials to be integrated in carbon-based HTM-free PSC. The objectives of this work are as follows:

i.   To investigate the emission decay rate of the blended organic long persistent luminescence (OLPL) materials (i.e., TMB and PPT) for the application in PSCs

ii. To assess the performance of carbon-based hole transport layer-free PSCs with the incorporation of blended OLPL materials.

iii. To evaluate the effect of blended OLPL materials to the charge kinetic of carbon-based hole transport layer-free PSCs

1.4 Novelty of Study

Most of the recent work on PSCs has been dominated by absorber material methylammonium iodide. Despite that, this material has its disadvantages such as stability issues that it degrades rapidly in ambient air. Mixed cations based on FAMAPbI$_3$ exhibit more stability compared to MAPbI$_3$ because of larger size of the

8

FA^+ cation contributes to a more stable crystal structure. Secondly, the high energy consumption of expensive hole-transport layers and fabrication of noble metal counter electrodes make them unfavorable for wide-scale production. Therefore, in this work, a series of HTM-Free PSCs ($FA_{0.4}MA_{0.6}PbI_3$) has been prepared in which carbon paste has been employed as a counter-electrode. Moreover, as explained above, this LPL material can illuminate in the dark. Unfortunately, research on OLPL materials and their applications in SCs, especially in emerging PV technologies such as perovskites, remains limited. This work aims to fill up this gap by focusing on the unique properties of OLPL materials and their incorporation into the structure of SCs, observing their effect on the performance of PSCs. Additionally, this work also focuses on exploring the unique properties of these LPL materials through various characterization techniques, including photoluminescence, time-resolved photoluminescence, and UV-VIS absorbance analysis.

1.5 Dissertation Outline

This dissertation paper contains 5 chapters. Chapter 1 briefly introduces the background of perovskite, a general introduction to PSCs, and their current device operational instability issues caused by humidity, and an overview of organic and ILPL. Chapter 2 provides the literature review that is relevant to this work, namely various kind of HTL, their approach, and outcomes. Photovoltaic cells with inorganic long persistent luminescence material (ILPL) and their afterglow. Chapter 3 discusses the methodology of the experiments and workflow i.e experimental procedure of

blended LPL, synthesis of FAMAPbI$_3$, and synthesis of c-TiO$_2$/m- TiO$_2$ in the PSCs assembly. Chapter 4 discusses the findings of ILPL, performance testing PSCs with or without LPL, and lastly the stability analysis throughout the period. Chapter 5 provides the conclusion and future recommendations of this research.

CHAPTER-2

LITERATURE REVIEW

2.1   Introduction

Over the past few years, PSCs are the most promising next-generation solar technologies due to their remarkable advancements. Generally, there are 5 main components in PSCs: perovskite light-absorbing layer, an electron transporting layer (ETL), a hole transporting layer (HTL), cathode electrode, and anode electrode as described in section 1.1. Further, PSCs are categorized as regular n-i-p and inverted p-i-n structure, based on which transport material (ETL/HTL) on the perovskite's surface initially comes into contact with light.

The n-i-p configuration contains mainly three layers: ETL, perovskite layer, and HTL. The n-i-p configuration has three layers: the ETL also called as n-layer, the intrinsic perovskite layer, and the HTL. Typically, the n-layer is composed of titanium dioxide (TiO_2), a material that efficiently collects and transports electrons to the bottom contact. A light-absorbing layer of perovskite is deposited between the ETL and HTL and generates electrons and hole pairs when excited by light. Lastly, the HTL, which is generally made from materials like spiro-MeOTAD, collects and transports holes to the top contact as shown in Figure 2.1 (a) (Yan et al., 2024). In contrast, in the p-i-n configuration, the layers are positioned in reverse

order, with the hole transport layer first, followed by the light-absorbing perovskite layer, and finally, the electron transport layer as shown in Figure 2.1 (b). In comparison to the mesoscopic n-i-p structure, p-i-n configuration shows higher open-circuit voltages and current densities. The density-voltage hysteresis of planar n-i-p PSCs is a major drawback. Furthermore, the p-i-n configuration can reduce the hysteresis in the current-voltage characteristics of PSCs, resulting in more stable and reliable device performance (Caprioglio et al., 2019).

At present, spiro-MeOTAD is the most widely used HTL despite its inherent shortcomings i.e poor conductivity, hygroscopic nature, and mismatched energy alignment (Suresh & Chandra, 2021). The most important it is expensive in nature which overall affects the cost of PSC. Therefore, a carbon- based HTL free PSC is proposed to avoid the use of expensive spiro-MeOTAD. Apart from its favourable electrical qualities, carbon possesses the ability to operateas an electrocatalyst.
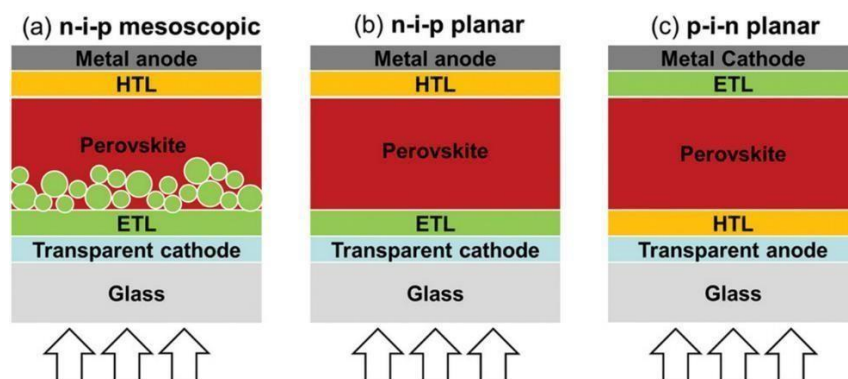
Figure 2.1 Schematic of (a) n-i-p mesoporous (b) n-i-p planar (c) p-i-n planar (Yan et al., 2024)

2.2 Carbon-based HTM-Free PSCs

Carbon-based PSCs (C-PSCs) free from HTL have attracted a lot of attention because of their exceptional stability and easier fabrication procedure. However, the absence of hole transport is significantly limited by the inadequate contact between the carbon electrode and the perovskite layer in planar-structured HTL-free C-PSCs, which directly hinders the fill factor from getting its highest value of the carbon-based PSCs. In a work by Zhang et al., (2020), to enhance the interface between the perovskite and carbon, they created a pressure-assisted technique that included modulating the applied pressure as shown in Figure 2.2 (a). The hot-pressing process increased the performance from 5.1% (normal) to 6.9% (HTM-free PSCs). Overall, the HTM-free PSCs derived from the hot-pressing method presented in their study show excellent promising opportunities to improve the efficiency of C-PSCs.
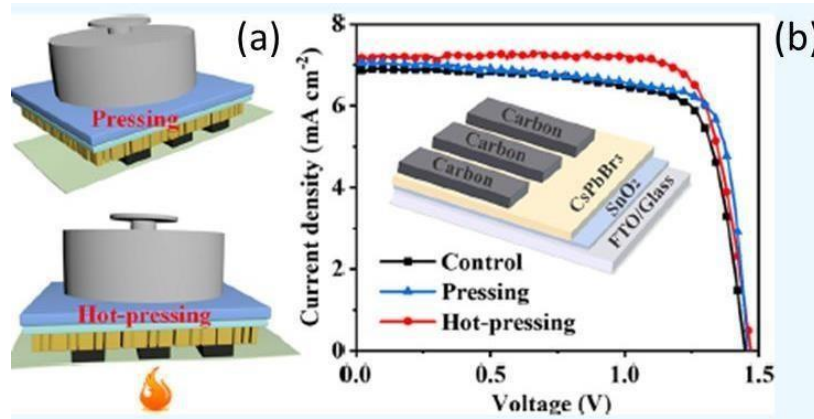
Figure 2.2 (a) Hot pressing of planar n-i-p PSCs (b) J−V characterization of the PSCs (Zhang *et al.*, 2022)

FTO/TiO$_2$/ZrO$_2$/C mesoporous scaffold constructed HTM-free C-PSCs were initially processed at 500 ^{o}C as reported by Han et al., (2013). Their studies reveal at the TiO$_2$/perovskite/carbon interfaces, the mesoporous structure facilitates effective charge transfer, resulting in a PCE of 6.64%. In recent years, continuous attempts have been made by researchers which resulted the efficiency of this type of mesoporous C-PSC device to exceed 17 % (Du et al., 2022 ; Chen et al., 2021). Recently, an alternate planar structured HTL-free PSCs with low-temperature processing of SnO$_2$ (150 ^{0}C) as the ETL has emerged (Chen & Yang, 2019). Despite that, the lack of a mesoporous scaffold in SnO$_2$-based C-PSCs results in a lack of charge transfer at the interfaces between SnO$_2$/perovskite (Yang et al., 2021). Consequently, for the high-efficiency planar structured HTL-free C-PSCs, a boost up of interfacial charge transport is very essential.

Compared to conventional hole transport materials, carbon-based materials like carbon nanotubes (Habisreutinger & Blackburn, 2021), carbon quantum dots (Tang et al., 2021), and graphene (Acik & Darling, 2016), are frequently more affordable in PSCs, which result in cost reduction of PSCs fabrication. Carbon-based hole transport-free designs often involve simplified device fabrication and processing methods, resulting in better stability, and potentially reducing degradation of perovskites (Li et al., 2014 ; Li et al., 2014) formed a network of carbon nanotubes and deposited it on a CH$_3$NH$_3$PbI$_3$ substrate using chemical vapor deposition technique but the drawback is that it needs high temperatures of 1150°C to prepare the carbon nanotube network.

In the context of this drawback, (Zhou et al., 2004) reported the fabrication of entirely solution-processable low-cost $TiO_2/CH_3NH_3PbI_3/C$ heterojunction SC based on a low-temperature-processed carbon electrode as shown in Figure 2.3(a). The C-electrodes were deposited by the doctor-blade technique. The entire device demonstrated high stability up to 2500 hours with a PCE of around 6.9% (Figure 2.3(b)) without any encapsulation. Additionally, it was noted that there was less charge recombination at the interface between the carbon and perovskite phases.
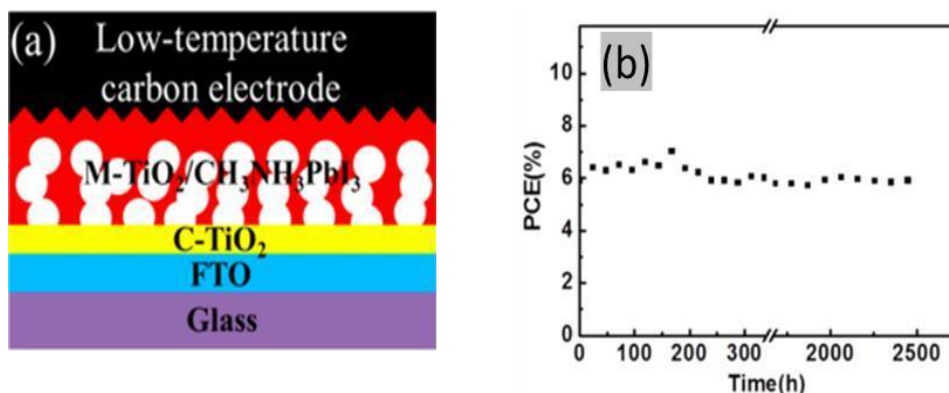
Figure 2.3 (a) Schematic architectures of C-PSCs (b) PCE vs time without encapsulation (Zhou et al., 2014)

2.3 Different Studies of Electron Transport layers

2.3.1 Tin Oxide (SnO₂)

In PSCs, electron transport layers (ETLs) facilitate electron transport efficiently during sunlight absorption. Its primary function is to extract electrons

from the perovskite layer, transport them to the electrode (typically the cathode), and prevent their recombination with holes. A well-designed ETL enhances overall device performance, efficiency, and stability. There are various types of ETL available such as TiO_2, SnO_2, ZnO and [6,6]-phenyl C61 butyric acid methyl ester (PCBM). In planar structures, conventional ETLs like TiO_2 are not very effective in extracting charge from the interface. They require very high temperature, typically around 500 ^{o}C for annealing. The high-temperature annealing removes defects within the TiO_2 layer, resulting in a more uniform and defect-free interface between the perovskite layer and ETL (Kim et al., 2017). However, TiO_2-based devices experience significant degradation when exposed under UV light. In comparison, SnO_2 exhibits a higher chemical stability, especially when subjected to UV light. Additionally, SnO_2 has a higher electron mobility which leads to more efficient charge transport and extraction. The enhanced mobility makes the device more stable and performs better (Uddin & Yi, 2022).

Ke et al., (2012), first described the sol-gel approach in which a low-temperature solution-processed technique for depositing a thin SnO_2 layer as an ETL in planar heterojunction PSCs. (Jiang et al.,2016) reported a highly effective ETL with a PCE of over 20% where solution-processed SnO_2 film was used. Despite the excellent advantages of SnO_2 films, it exhibits defects or trap states, resulting in non-radiative recombination of charge carriers and a decrease in the overall performance of the device. In a work by of (Ma et al.,2015 ; Dong et al., 2015), a nanocrystalline SnO_2 as ETL was employed in PSCs (S-PSC) and

performance was compared with TiO$_2$-based PSCs (T-PSC). Their device exhibited a higher short-circuit current density but lower open-circuit voltage and lower fill factor than conventional TiO$_2$-PSCs. Consequently, the PCE of S-PSC was superior to T-PSC. The devices exhibited a comparatively low fill factor (FF) and open-circuit voltage (V$_{OC}$).

2.3.2   Zinc Oxide (ZnO)

ZnO is a semiconductor that shows a promising agent as an ETL because ofits large band gap and better electron mobility compared to TiO$_2$, and it can be easily deposited on a conducting substrate without high-temperature annealing (Qiu et al., 2022). In a study by Mahmud et al.,(2017), the best PCE was 8.77% when ZnO was deposited as ETL and processed for 60 minutes at 140 °C, which explained that ZnO is the suitable material for ETL. However, in some of the studies it was found that organic/inorganic perovskite film can degrade into PbI$_2$ when directly deposited on the ZnO layer, leading to the appearance of a yellow color. A similar phenomenon was found by (W. Huang et al., 2021), found that MAPbI$_3$ films decomposed into a yellow-colored (Figure 2.4 (a)) byproduct when MAPbI$_3$ was employed over the ZnO layer. As a result, the efficiency of PSCs was very low due to their moisture-sensitive nature. Although, ZnO has demonstrated the ability to operate as an ETL even at low processing temperatures. Because of its tendency to react with MAPbI$_3$, it should be used with caution in PSCs.
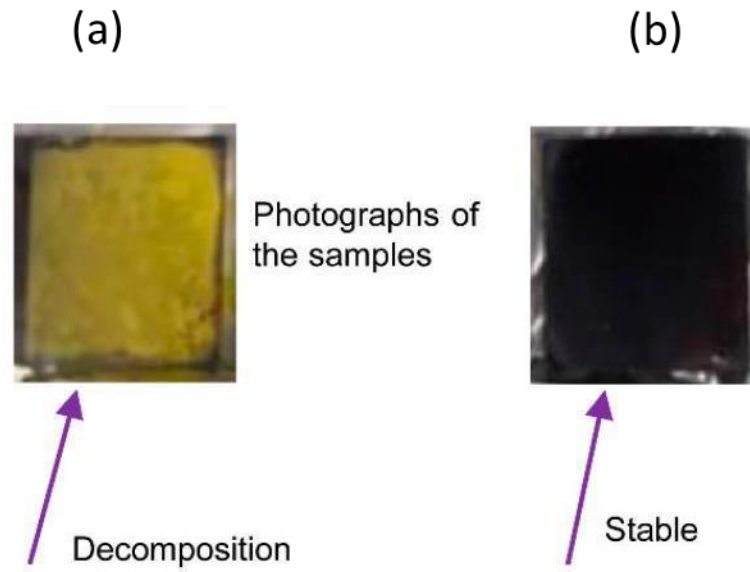
Figure 2.4 (a) Degradation of Perovskite Film (b) Stable Perovskite Film (W. Huang *et al.*, 2021)

2.3.3 Titanium dioxide (TiO2)

TiO$_2$ is well renowned for being stable and works well with perovskite materials due to its strong chemical stability, high transparency, and favorable bandgap to perovskites. An annealing temperature of greater than 400 °C is necessary for conventional mesoporous TiO$_2$ structure in order to obtain suitable crystallization (Malevu et al., 2019). It was found that annealing at high temperature significantly improves the surface smoothness, density of grain boundaries, and carrier mobility of TiO$_2$ film as a result of enhancement in PCE (Xue et al., 2023). According to (Li et al., 2020) a hydrothermal method was used to grow an array of anatase-phase TiO$_2$ nanorods on a conductive substrate, resulting in a 15.3% efficiency in PSCs.

18

There are currently numerous ways to fabricate compact (c-TiO₂) that have been proposed in the early literature, including atomic layer deposition (Di Giacomo et al., 2015), spray pyrolysis (Saliba et al., 2016), electrochemical deposition (Kavan et al., 2014), and spin-coating (Im et al., 2014). Specifically, spin-coating is extensively utilized in PSCs because of its affordability, simple deposition, and convenience. Nowadays, the optimization of the compact layer continues to get a lot of interest by researchers. In a work by Shahiduzzaman et al., (2020), low- temperature TiO₂ was deposited as ETL via spin coating technique in their traditional planar PSC. They prepared the C-TiO₂ solution by mixing hydrochloric acid added isopropanol in TTIP precursor and annealed at 150 °C for 45 min. Because of its low annealing temperature, the ETL of TiO₂ suffered from high trap states, which led to low PCE.
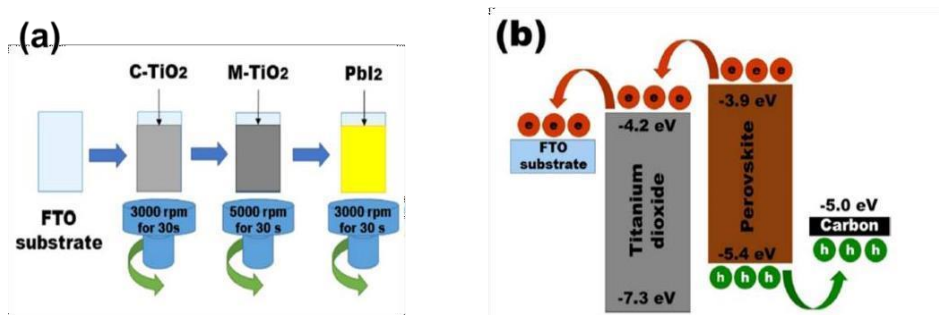
Figure 2.5 (a) Deposition of c-TiO2/m-TiO2 (b) Energy level diagram of PSCs with TiO₂ (Shahiduzzaman et al., 2020)

Further, in a work by (Shahiduzzaman et al., 2020), TTIP and HCL diluted in ethanol were spin-coated at 3000 rpm for 30 s and annealed at 500 °C for 30 mins to deposit the compact TiO₂ layer. Similarly, mesoporous-TiO₂ (m-TiO₂) film, the solution of the diluted TiO₂ paste was spin-coated at 5000 rpm for 30 seconds,

followed by heating at 500 °C again for 30 mins as shown in Figure 2.5(a). Their findings showed that employing high temperatures to anneal TiO_2 as an ETL produced the best PCE of 8.81%.

2.3.4 ETL Comparison

As explained above, among the various electron transport layers used in PSCs TiO_2 is particularly suitable for various reasons. Primarily, TiO_2 shows excellent chemical stability, providing long-term durability and reliability for PSCs. Moreover, TiO_2 has a band alignment that is well suited to the perovskite absorption layer, which makes electron extraction easier and reduces the chance of charge recombination. This ideal band alignment maximizes the collection of photogenerated charge carriers, which improves the overall efficiency of the device (Etacheri et al., 2015). In contrast to TiO_2, alternative ETL materials such as SnO_2 and ZnO present certain disadvantages that limit their widespread adoption, leading to non-radiative recombination of charge carriers (Hoang Huy & Bark, 2023). Similarly, ZnO is hydrophobic in nature, due to this the interface between perovskite and ETL may be hindered and can affect the overall performance. Therefore, ZnO is not compatible with certain processing techniques or substrates commonly used in PSCs fabrication (Azmi et al., 2018 ; Zeng et al., 2020). Lastly, TiO_2 is still the material of choice for the electrothermal junction (ETL) in PSCs because of its stability, band alignment, and electron mobility. However, research is ongoing to address the drawbacks of other materials,

such as SnO_2 and ZnO, and to increase the number of options that can be used to improve device performance and stability.

2.4   Mechanism of organic luminescence

Figure 2.6 shows the working mechanism of OLPL phenomenon, when light strikes, LPL molecule gets excited from its ground state (S_0) to its excited state (S_1) and can move into a singlet or triplet state. It emits light right away in the singlet state as fluorescence. The triplet state emits light more slowly, and this delayed emission is called phosphorescence. Non-radiative decay may also occur. An excited molecule may occasionally interact with a surrounding molecule rather than immediately generating light. A charge-transfer state is produced by this interaction, in which electrons travel between molecules. After that, the charged molecules split apart to create states known as charge-separated states. In charge-transfer states, electrons move from the donor molecules HOMO to the acceptor molecules' HOMO during photo-excitation. After that, charge-separated states are formed when the acceptor radical anions disperse to separate the donor radical cations from the acceptor radical anions. There is a 25% singlet exciplex to a 75% triplet exciplex ratio produced by charge recombination of the TMB radical cations and PPT radical anions. In exciplex systems, reverse intersystem crossing (ISC) by thermal activation is made possible by a small energy difference between the lowest singlet excited state (S_1) and the lowest triplet excited state (T_1). This small energy

means light is produced, and it can last for a long time, giving us organic long persistent luminescence (Shanker et al., 2015)
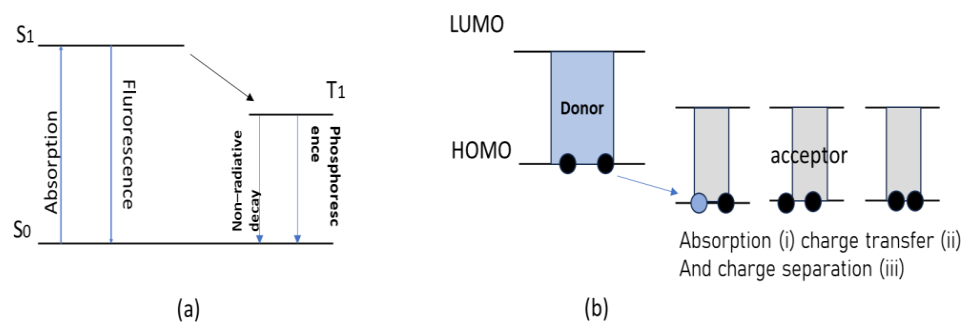
Figure 2.6 (a) Molecule excitation (b) Stages of charge carriers (Kabe and Adachi, 2017b)

2.5   LPL in SCs

Long-persistent luminescence (LPL) or long-persistent phosphors (LPP) materials can capture and store energy during periods of abundant light and gradually emit it later. This characteristic enhances the overall energy collection capacity and reliability of the energy storage photovoltaic module. Therefore, some research has concentrated on incorporating LPL materials into SCs to utilize the stored persistent luminescence to continue producing power during the night. In a work reported by Riaz et al., (2022), they developed all-weather solar cells using graphitic carbon nitride nanotubes and green-emitting LPL material (Figure 2.7 QDSC device structure with LPP). The PCE in sunlight was 18.5% in that quantum dot SC which is regarded as good. Unfortunately, in low light conditions, no noticeable power outputs were detected. However, this investigation demonstrated

that the PV devices' daylight performance was enhanced by the addition of ILPL materials.
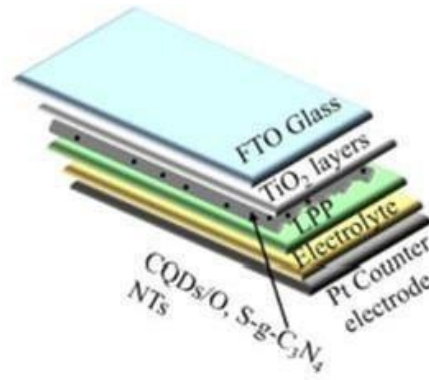
Figure 2.7 Quantum Dot SC with LPP (Riaz et al., 2022)

Similarly, in a work by (Deng et al., 2020), a bifunctional structured layer made of LPL $SrAl_2O_4$:Eu,Dy, and CdSe quantum dot-sensitized TiO_2 was employed as shown in Figure 2.8. The LPL materials were used in their study as a layer integrated into the cell, where the layer was coated over a transparent nanostructure TiO_2 layer that had been sensitized with CdSe quantum dots. According to the results, the cell's performance was boosted by 48% as compared to when the LPL materials weren't used. Under dark conditions, the device was able to generate electricity at a low efficiency of 0.04% because of the afterglow effect of the LPL. Despite its poor performance in the dark, the integration of LPL enhanced the device's performance during the daytime (Deng et al., 2020). They found a similar observation when they applied several kinds of LPL in CdS/CdSe quantum dot-sensitized SCs (QDSSCs).

A 24% improvement in PCE was noted for devices that had more LPL. These devices can even operate in the dark with a small period of illumination.
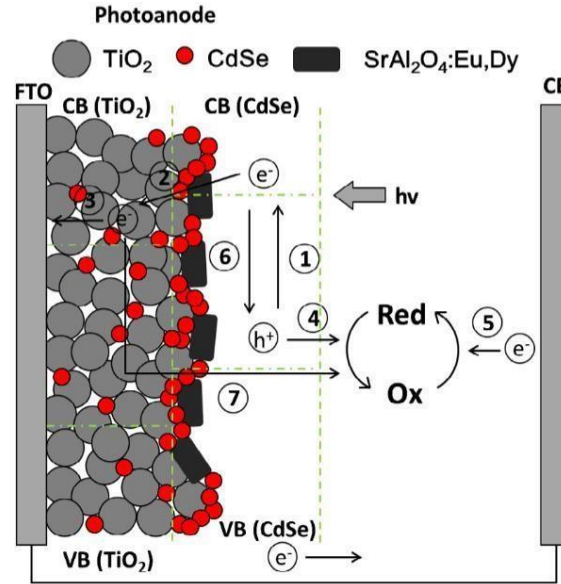
Figure 2.8 Schematic diagram of the bifunctional structured of LPL and

CdSe quantum dot-sensitized SC (Deng et al., 2020)

In a work by S. Huang et al. (2021), $CaAlSiN_3:Eu^{2+}$ (CASN) and $Y_2O_3:Eu^{3+}$ (YO) phosphors were mixed with ethyl vinyl-acetate (EVA) to form luminescence films shown in Figure 2.9 which are used to improve crystalline silicon solar cells by converting the photons with the wavelength. These films are used to enhance crystalline silicon solar cells by converting photons at specific wavelengths. Their findings demonstrate that shows that the conversion efficiency of the solar cells increased from 19.61% to 20.00%.
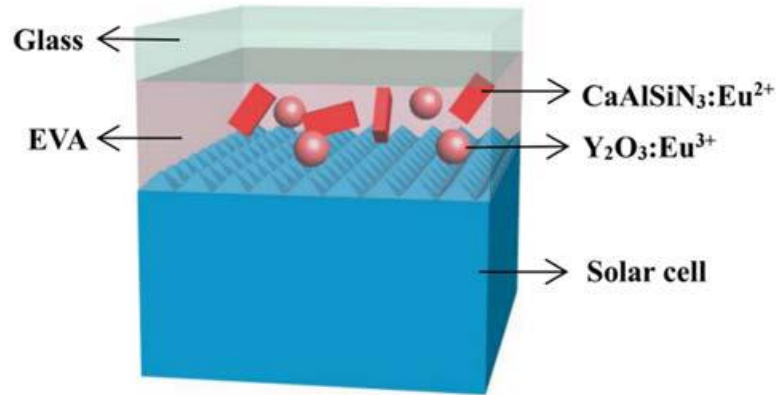
Figure 2.9 SC with CASN and YO phosphors (S. Huang et al., 2021)

2.6 Conclusion from the literature review

As described in the previous sections, it can be concluded that not all SCs are capable of achieving high efficiency. To boost their efficiency, scientists and engineers are looking at novel materials and manufacturing processes. The most challenging problem in PSCs is to address the poor performance due to the rapid degradation that occurs once it comes in contact with moisture. Moreover, it is well-known, that SCs work only when there is a sufficient amount of sunlight present, which is not available when and where it's needed at night. Consequently, energy storage technologies such as batteries and pumped hydro storage are needed as backups to provide a continuous and reliable supply of electricity. This issue can be resolved by using LPL materials in SCs, which allow for emission in the dark (Sibiński, 2023). Persistent luminescent materials have the ability to retain energy after being excited by a light source, which allows them to release light gradually. This method can enhance the cells' functionality and efficiency, particularly in low-light conditions. Unfortunately, the uses of LPL materials in SC devices are quite

25

restricted as compared to other well-established SC technologies such as silicon or PSCs. Consequently, it is important to investigate the compatibility of LPL materials with perovskite materials used in SCs and to make sure that the integration of LPL materials does not compromise the stability or performance of the SC. Therefore, based on the previously reported studies with other types of SCs, LPL materials can be also integrated with PSC as shown in Figure 2.10. The detailed optical studies and feasibility of such integration have been demonstrated in this work.
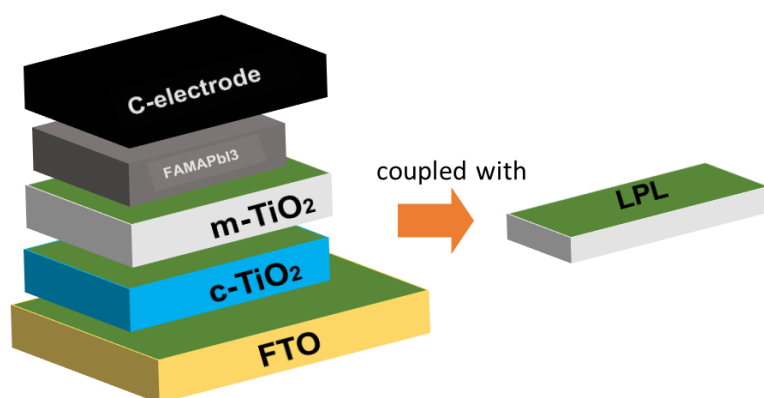
Figure 2.10 Proposed Schematic of PSCs with LPL

CHAPTER-3

METHODOLOGY

3.1 Raw Material

The material required for the fabrication of PSC are listed in Table 3.1 below. All materials were used as received except for FTO glasses, where cutting and cleaning were performed.

Table 3.1 List of raw materials

Material	Role	Brand
3,3',5,5'-Tetramethylbenzidine	Organic Luminescent	Sigma-Aldrich
2,8 Bis(diphenylphosphoryl)dibenzo[b,d]thiophene	Organic Luminescent	Sigma-Aldrich
Conductive FTO glass	Photoanode	Greatcell Solar
Titanium isopropoxide	Electron transport layer	Sigma-Aldrich
Mesoporous Titanium(IV) Oxide Paste	Interface for perovskite	Greatcell Solar
Isopropanol, Ethanol	Solvents	Merck Millipore
2 M Hydrochloric acid	Doping Element	Merck Millipore
Formamidinium Iodide	Organic Cation	Sigma-Aldrich
Lead(II) iodide	Metal, halogen	Sigma-Aldrich

Methylamonium Iodide	Organic Cation	Sigma-Aldrich
Dimethyl sulfoxide (DMSO)	Solvent	Sigma-Aldrich
Dimethylformamide (DMF)	Additive	Merck Millipore
Carbon paste	Counter electrode	Dycotec Materials

3.2 Etching and cleaning of FTO glass

The FTO glass was cut into the size of 18 mm×14 mm. The high temperature PVC tape was stuck at the edge of the glass on the conducting plane of FTO. Then Zn powder was spread on the glass, and then diluted hydrochloric acid (2M) was dropped onto the Zn powder to FTO layer where it is not protected by the conductive tape. The zinc powder reacts with the FTO layer, particularly the tin (Sn) component, forming soluble zinc tin compounds (such as $ZnCl_2$) through a redox reaction. This reaction helps in removing tin from the FTO surface. As a result, the surface becomes cleaner and more conducive for the subsequent deposition (Triana, Kusumandari and Suryana, 2016). Similarly, HCl reacts with the FTO surface, particularly the tin oxide component, to dissolve and remove any surface contaminants, oxides, or residual organic materials. HCl further cleans the FTO surface, dissolving contaminants and oxides, and preparing it for subsequent deposition processes (Haghighi et al., 2023). The purpose of etching is to remove the oxide layer on the surface of the substrate and make the surface smoother, thereby improving the adhesion and quality of the film deposition over it. After etching, clean the Zn powder with a cotton swab, then the high-

temperature tape was taken off. The etched FTO substrate was ultrasonicated in deionized water, decon90 detergent, and rinse the substrates (3-4 times) followed by distilled water and isopropanol for 20 min. Then the FTO substrates were heated at 150 °C for 10 min. Finally, the FTO substrate was treated in UV-Ozone cleaner for 20 min. The etched FTO glass surface is meant to be further cleaned and activated by using a UV ozone cleaner. UV ozone cleaners generate both UV light and ozone (O_3), which together remove any remaining contaminants from the FTO substrates.

3.3   Preparation of LPL

In the active phase, two OLPL samples were used namely N,N,N′,N′-tetramethylbenzidine (TMB) and 2,8 bis(diphenylphosphoryl)dibenzo[b,d]thiophene (PPT) which were mixed in various ratios as shown in Table 3.2. The TMB has high luminescence efficiency (Dong et al., 2021). PPT is another organic luminescent material chosen for its excellent stability under an inert atmosphere (Jeong and Lee, 2011). The TMB functions as an electron-donating molecule and the PPT functions as an electron-accepting molecule to create the prolonged charge-separated state. The blend was then subjected to a melting process at 220 °C on a quartz substrate, and subsequently, epoxy encapsulation was applied to shield it from moisture. Once the material melted, it was immediately treated under UV lamp to examine the self-illumination as shown in Figure 3.1.

Initially, two organic compounds—TMB and PPT—were selected for the preparation of long persistent luminescence (LPL) materials. When PPT was

handled, it became apparent that it was extremely sensitive to moisture and stuck to glass vial tubes quickly, making it challenging to transfer the exact quantity required. Consequently, in order to resolve this problem, the weighing procedure was carried out in an inert argon environment inside a glovebox. The PPT powder was precisely weighed in various ratios in this controlled atmosphere, and it can be transferred onto microscopic glass slides without disturbing the risk of moisture interference. This process made sure that our samples were consistently measured precisely. For accuracy purposes, other heating and characterization procedures were carried out at room temperature to obtain consistent results.
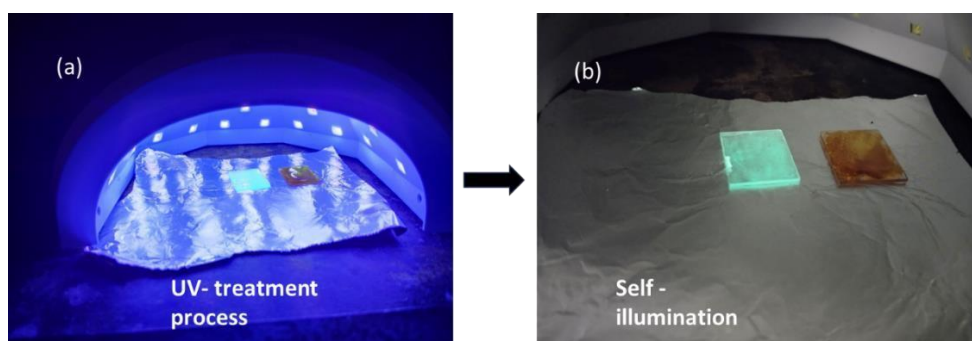
Figure 3.1 Picture of LPL material (a) UV treatment under UV Lamp (b) Self- illumination

Table 3.2 Composition of TMB and PPT for cell-1 to 5

S. No	Sample	Ratio	Mass of TMB (mg)	Mass of PPT (mg)	Total mass (mg)
----	Pure TMB	1:0	50	0	50
----	Pure PPT	0:1	0	50	50
Cell-1	TMB + PPT	1:1	50	50	100
Cell-2	TMB + PPT	3:2	60	40	100
Cell-3	TMB + PPT	7:3	70	30	100
Cell-4	TMB + PPT	4:1	80	20	100
Cell-5	TMB + PPT	9:1	90	10	100

3.4 Preparation of compact TiO_2 solution

In order to make compact TiO_2, Initially, 369 μl of titanium isopropoxide (TTIP) was diluted with 2.53 ml of isopropanol. On the other hand, 2M HCl solution (35μl) with 2.53 ml of isopropanol was mixed together to achieve the concentration of 0.026 M. Lastly, while dynamically stirring, the acid-containing solution (2M HCl) was gradually mixed with the titanium precursor solution. Then, the entire solution was then completely filtered using a 0.25 m PTFE filter (Qin et al., 2017). It is anticipated that the resulting TiO_2 layer would have a uniform, smooth surface, which is essential for reducing defects and promoting effective electron transport. The smooth and dense structure of this compact TiO_2 layer serves as an electron-selective contact, preventing electron recombination at the interface. Its compact nature is essential for creating an effective barrier, thereby enhancing the overall efficiency of PSCs (Wang et al., 2014).

3.5   Preparation of mesoporous TiO₂ solution

To obtain a mesoporous TiO_2 layer, TiO_2 paste was diluted in ethanol with a ratio of 1:3.5 (wt%) and spin-coated on an FTO substrate under the same conditions as the blocking layer, and annealed at 250°C for 10 minutes and 450°C for 30 minutes (Pospisil et al., 2020) as shown in Figure 3.2(b). This procedure produces a high-porosity layer that gives the perovskite material a broad surface area, promoting effective electron transport and lowering recombination losses. Similarly, it is also anticipated that the mesoporous TiO_2 layer would have a high porosity, which offers a large surface area for perovskite absorption as well as effective electron transport. These features are essential for optimizing the SC's efficiency and performance.

3.6   Preparation of Perovskite Precursor

In order to prepare perovskite $FA_{0.4}MA_{0.6}PbI_3$ precursor solution, 0.4 M of formamidinium iodide (FAI), 0.6 M of Methylammonium iodide, and 1 M of lead iodide (PbI_2) were dissolved in 600 µl of dimethylformamide (DMF) and 71 µl of dimethyl sulfoxide (DMSO). The precursor powders were weighted inside an argon glovebox to avoid contamination the stock PbI_2, FAI and MAI chemicals with outside air and moisture (Figure 3.2). The weighted powder was then transferred outside and quickly dissolved in the prepared solvents in order to reduce contact with the moisture and oxygen in the surrounding air. The solution was well stirred

with a magnetic stirrer for 15 to 20 minutes at room temperature, or until a translucent yellowish color appeared. In a study by (Duan *et al.*, 2018) has validated that the $FA_{0.4}MA_{0.6}PbI_3$ composition leads to perovskite films with superior morphological and electronic properties. As a result, the concentrations of FAI, MAI, and lead iodide PbI_2 were selected after a thorough literature study. The solvents dimethylformamide (DMF) and dimethyl sulfoxide (DMSO) were chosen because of their high boiling point and capacity to efficiently dissolve perovskite precursors. By allowing enough time for crystal development during the annealing process, high boiling point solvents like DMF and DMSO aid in the formation of a homogeneous perovskite coating. In addition, 2% DMSO was added to the precursor solution in order to fully convert PbI_2 into the perovskite structure (ABX_3). This addition aids in achieving better film morphology and improved device performance by ensuring complete crystallization and minimizing defects. This whole process was performed under dark to prevent light interaction. Lastly, the entire precursor solution was filtered by using 0.25 µm PTFE syringe filter to remove any undissolved impurities and to obtain a fully transparent perovskite precursor.
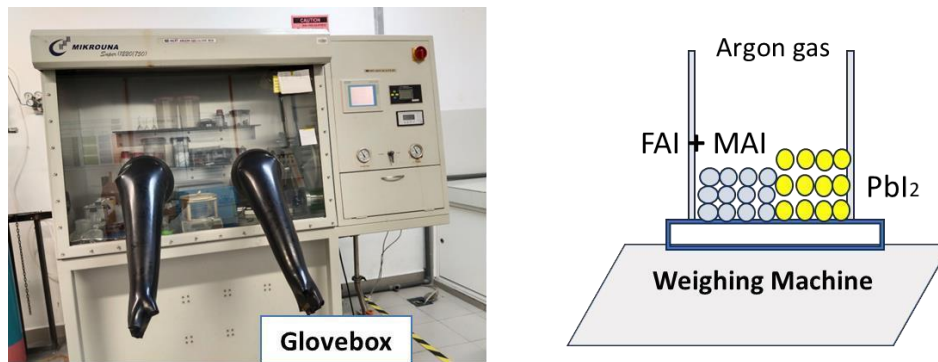
Figure 3.2: Representation of FAI, MAI and PbI₂ weighed inside an argon glovebox

3.7   Assembly of PSCs

The schematic fabrication procedure of PSC is shown in Figure 3.3. In order to form a c-TiO$_2$ layer on the FTO substrate, the first step was to spin-coat a 50 μL of prepared TiO$_2$ solution (section 3.4) on the FTO substrate at 3000 rpm for 30 seconds and then anneal it at 450 °C for 30 minutes as shown in Figure 3.4(a). In order to avoid direct contact between the perovskite layer and the FTO substrate, the c-TiO$_2$ layer functions as a blocking layer. In the same manner, the m-TiO$_2$ layer was covered with a mesoporous TiO$_2$ layer by spin-coating a diluted TiO$_2$ paste solution for 30 seconds at 5000 rpm (Figure 3.4 (b)). Again, TiO$_2$-coated FTO glass was kept for annealing at 250 °C for 10 minutes, followed by 450 °C for 30 minutes in order to achieve the formation of a stable and well-ordered crystal structure (Parashar & Kaul, 2021). This m-TiO$_2$ layer offers a high surface area resulting in increase the interface area for charge separation and improved electron transport.

For the absorption layer, 60 μL of perovskite solution containing double cation perovskite precursor ($FA_{0.4}MA_{0.6}PbI_3$) was spin-coated over the mesoporous-TiO$_2$ (m-TiO$_2$) oxide layer. Subsequently, followed single-step spin-coating method at room ambient conditions, with 1000 rpm for 18 s, then 4000 rpm for 18 s (Figure 3.4 c). To produce uniform and smooth surfaces, thin layer formation in both the TiO$_2$ and perovskite films depends on the spin-coating rates. In order to minimize defects and ensure consistent device performance, uniform films are essential. Therefore, a lower spin-coating speed (1000 RPM) allows the precursor solution to spread evenly. In the next step, a higher spin-coating speed (4000 RMP) helps to maintain the minimum thickness.

Additionally, the substrate was placed in a chamber attached to a vacuum pumping device in order to undergo the vacuum-flash solution processing (VASP) treatment, which was utilized as an anti-solvent approach to get a reflective and shiny surface for the perovskite layer. The substrate was then removed from the chamber after returning to normal atmospheric pressure and quickly placed on a hot plate at 120 ° C for 10 minutes in an ambient environment for annealing (Chen et al., 2019). This annealing temperature and duration are selected in order to ensure proper crystallization of the perovskite film. A proper annealing process ensures complete evaporation of the solvent and enhances crystallinity, which is crucial for effective charge transfer and high performance. The function of this obtained perovskite layer is to absorb the light. Following, the carbon black paste was applied directly to the perovskite layer using a doctor blade as the counter electrode, and it was cured for ten minutes at 120°C. The final schematic structure of the PCS sample is shown in Figure 3.4 (d). The role of this carbon electrode is to collects the holes

that the perovskite layer generates once it interacts with the light.
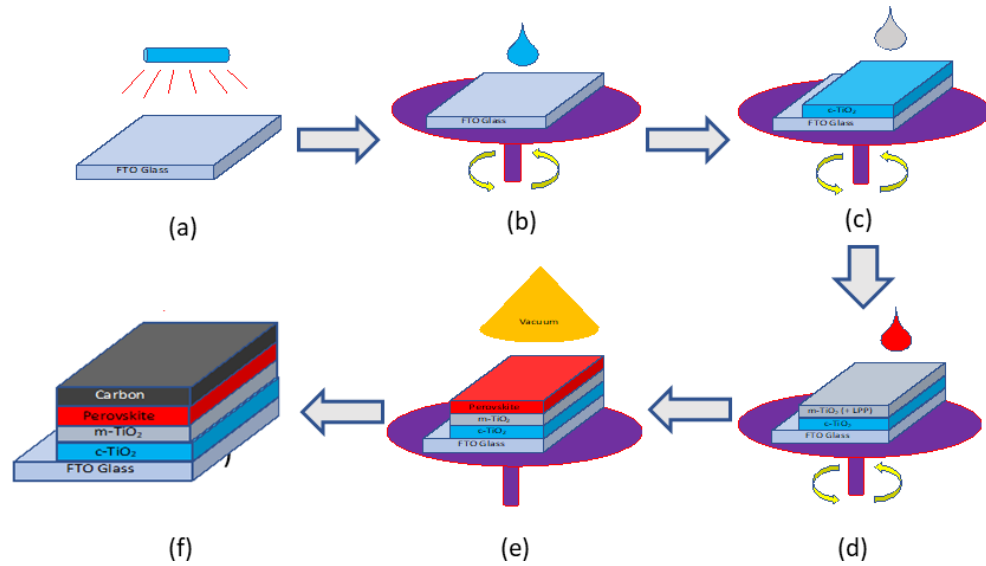
Figure 3.3 Step-by-step fabrication process for PSCs: (a) Ozone cleaning of FTO glass with light, (b) Deposition of c-TiO$_2$ layer, (c) Deposition of m-TiO$_2$ layer, (d) Deposition of FA$_{0.4}$MA$_{0.6}$PbI$_3$ layer (e) VASP treatment, and (f) Deposition of Carbon layer via Doctor's blade method

The durability and performance of PSCs can be greatly impacted by surface imperfections, pinholes, and non-uniformities at the interfaces. In the perovskite layer, these problems are frequent. In this work, an anti-solvent method called VASP treatment was used to overcome this difficulty. By using this method, the perovskite layer's surface was made uniformly reflective, which enhanced the SC's overall performance.

36
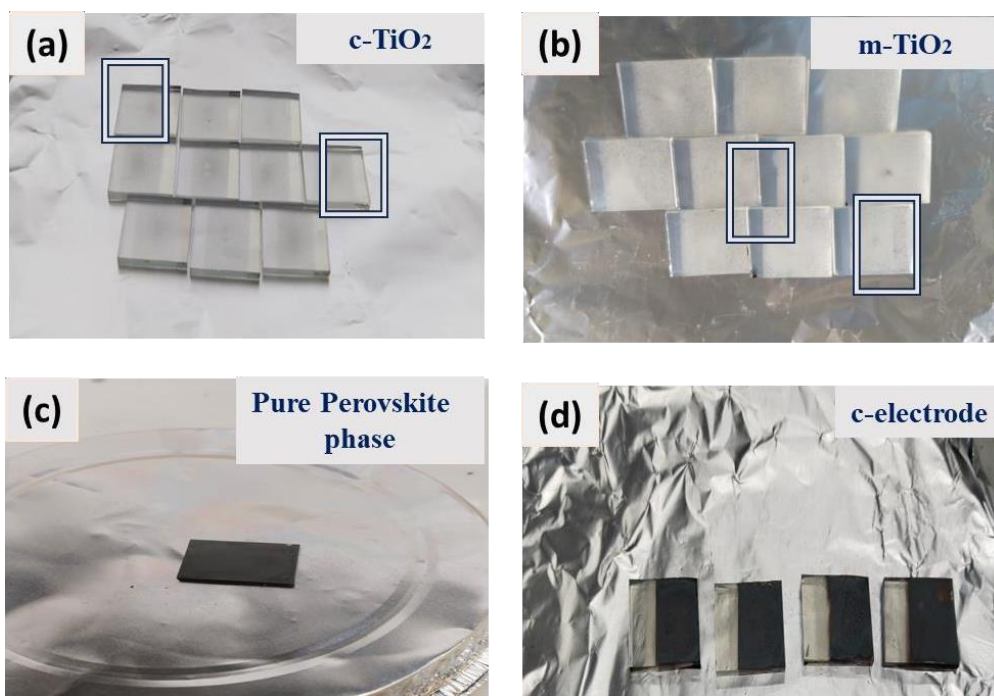
Figure 3.4 Different stages of PSC samples: (a) Coating of c-TiO₂ (b) Coating of m-TiO₂ (c) Pure Perovskite Film (d) Perovskite Samples covered with carbon electrode

3.8 Assembly of PSCs with LPL (L-PSCs)

In order to fabricate the L-PSCs, a novel approach has been adopted in which an active layer of LPL was externally coupled to the C-PSCs. The LPL layer was configured in two configurations: top-facing (Figure 3.5a) or bottom-facing (Figure 3.5b), positioned over the light source.

This approach made it possible to examine the effects of 2 different orientations of LPL layer on the general effectiveness and performance of the L-

PSCs. The objective was to maximize the SC efficiency and optimize light absorption. Later, the outcomes reveal that the LPL with the bottom facing has negligible performance. Therefore, the approach with top-facing L-PSC was chosen for all measurements.
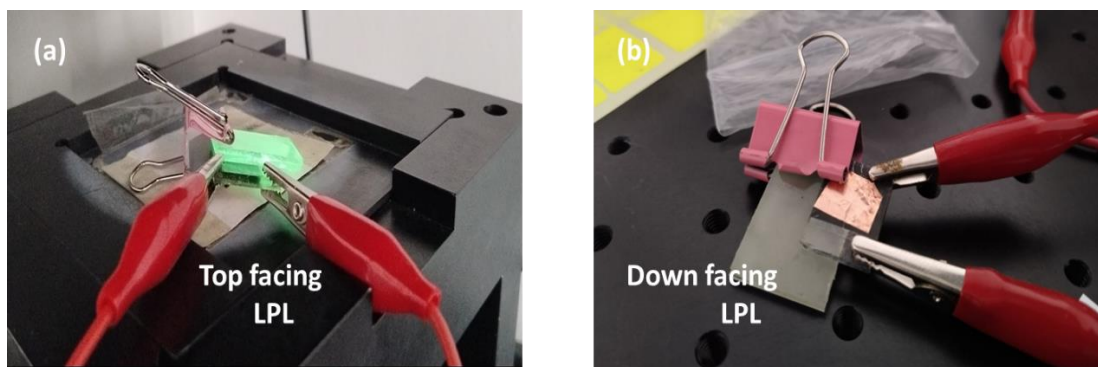
Figure 3.5 (a) PSC with top facing LPL (b) PSC with bottom LPL

3.9   Characterization

The UV-VIS (Ultraviolet-Visible) spectrum was performed ranging from 200-800 nm with a UV-VIS spectrophotometer (Varian, model no- EL07063063) to analyze the absorption of light by any material.

The XRD (X-ray diffraction) characterization was performed using X-ray diffractometer (model Shimadzu XRD-6000) to analyze the phase identity of perovskite and LPL. A detailed study of the surface morphology of perovskite film was observed under scanning electron microscopy (SEM) (Hitachi, model no-S3500) and field emission scanning electron microscopy (FESEM) (Hitachi, model no S5000N). Similarly, high-resolution transmission electron microscopy (HRTEM) was carried out to observe the fringe spacing of the perovskite structure.

The SC performance was evaluated through J-V characteristics with an solar simulator (using Keithley 2400 electrometer conducted under xenon lamp illumination of 100 mW m^{-2}) and electrochemical impedance measurement using potentiostat (Model Zive SP1) with frequency scanning range from 100kHz to 0.1 Hz). The efficiency of the SCs were calculated using the following equation:

$$\eta = (J_{sc}V_{oc}FF)/P_{in} \hspace{3cm} (3.1)$$

where J_{SC} is the photocurrent density at a short-circuit, V_{OC} is the open-circuit voltage and FF is the fill factor. P_{in} represents the light intensity.

CHAPTER-4

RESULTS & DISCUSSION

4.1   Introduction

Integration of LPL materials into PSCs offers a good opportunity to enhance their functionality and performance. The aim of this work was to investigate how OLPL materials affect the charge kinetics and efficiency of carbon based, HTL free PSC. The preparation of OLPL materials was the first step in the study, and then several techniques were used to conduct a thorough characterization. i.e UV- VIS analysis, photoluminescence spectroscopy, and time-resolved photoluminescence (TRPL) spectroscopy. Important details on the stability and optical characteristics of the OLPL materials were analyzed from these characterizations.

The LPL materials were incorporated into C-PSC once they were optimized. The perovskite material was thoroughly characterized using XRD, HRTEM, FESEM and SEM before OLPL integration. The performance of the PSC with and without LPL was then assessed via current-voltage (I-V) analysis. Finally, using EIS, the charge kinetics of the C-PSCs with OLPL and ILPL were examined.

4.2   Optical properties of LPL

Ultra-violet visible (UV-VIS) spectroscopy is used to study the optical absorption intensity of the material (with various ratios) which helps in identifying the optimized composition of OLPL (TMB and PPT) absorption edges and their respective band gaps. This range was selected because it covers both the ultraviolet (200-400 nm) and visible (400-800 nm) regions. Absorbance spectra in the UV and VIS regions of the electromagnetic spectrum provide vital information about a material's capacity to absorb light. According to this obtained data, the absorbance of the blend of TMB and PPT with a combined UV-Vis spectrum ranging from 200 nm to 800 nm has been analyzed. The absorbance spectrum is plotted for 7 cases with different ratios of TMB and PPT, whereas cell-1 to cell-5 are the blends of TMB and PPT with varying ratios as shown in Figure 4.1.
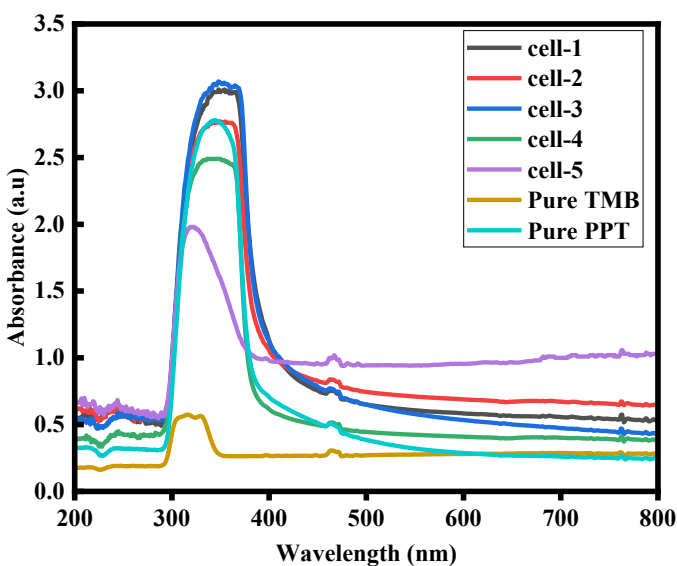
Figure 4.1 UV VIS spectra of LPP with different ratios of TMB and PPT.

It is clear from Figure 4.1 that, at a wavelength of 350 nm, cell-3 TMB: PPT (7:3) exhibits the highest absorption. The intensity of absorption rises with an increase in TMB concentration. The peak of cell-3 shows that its maximum absorption of light occurs at 350 nm. Also, certain chemical or electronic transformations taking place inside the material are indicated by this peak absorbance. The absorption at 350 nm is also seen in (Figure 4.1) pure TMB and PPT samples because of their short π-conjugation. At 394 nm and 346 nm, TMB and PPT both exhibited their peak fluorescence, respectively. In order to achieve long-lived charge-separated states, this work used the strong electron-donating chemical TMB, which contains a very stable radical cation (Doki et al.,2024). An increase in temperature will cause TMB oxidation, which will change the maximum absorbance. Without recombining to lose energy, the photo-generated radical cations and anions must accumulate in the blend. The bandgap of blended LPL (cell-3) using Tauc's method lies in between 3.06 – 3.50, and then based on the highest absorbance intensity, cell-3 comes out to be optimized composition and its corresponding Tauc's plot is shown in Figure 4.2 with a band gap of 3.17 (eV) as, which is calculated by using the equation:

$$E_g = 1240 / \lambda_{onset} \qquad (4.1)$$
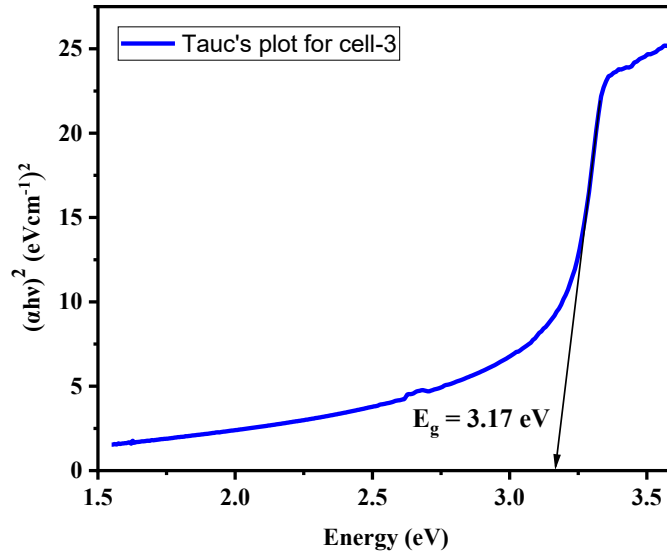
Figure 4.2 Tauc's plot for cell-3

Choosing a material to integrate into PSCs requires consideration of its band gap when compared to the absorbing layer on the perovskite. To optimize the SC's overall performance, the band gap of the additional material should match the perovskite layer's band gap. By absorbing light in a different region of the solar spectrum, it should be able to increase the total amount of sunlight absorbed and maximize efficiency (Teixeira et al., 2022). The Tauc's equation may be used to estimate the band gap in the following manner:

$$\alpha h\nu = A(h\nu - Eg)n \qquad (4.2)$$

where ν is the incoming photon frequency, A is the proportionality constant, h is the plank's constant, α is the absorbance coefficient, and Eg is the optical band edge. For the direct band transition, the value of (n) is ½.

4.3 Optical Properties of Perovskite

Like OLPL, the absorption spectrum obtained from UV-VIS spectroscopy shows how much light the perovskite material absorbs at different wavelengths. A material's band gap with the perovskite's absorbing layer must be taken into account when selecting it for integration into PSCs. The band gap of the inserted material must coincide with the band gap of the perovskite layer in order to maximize the overall performance of the SC.
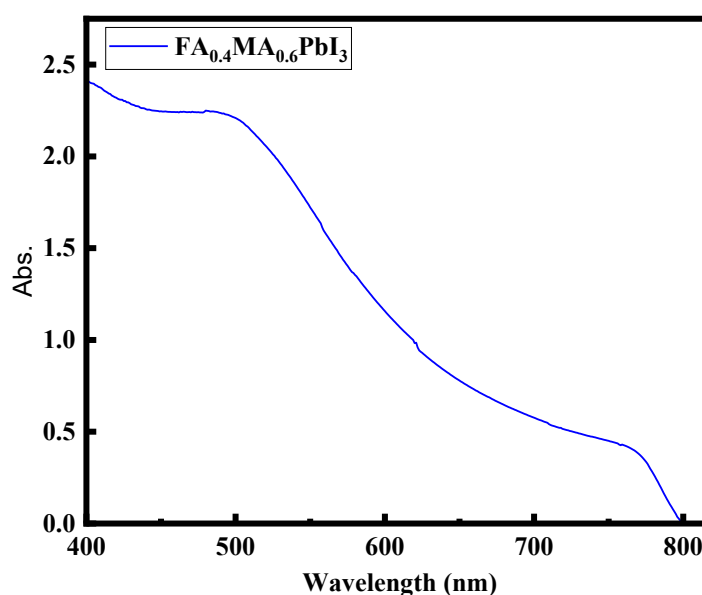
Figure 4.3 The UV-VIS absorption spectra of Perovskite

The UV-VIS absorption spectra of the perovskite film are displayed in Figure 4.3. The Longer wavelengths showed a decrease in intensity, which indicated the existence of induced states that cause the recombination processes occurring in the material (Wu et al., 2022).
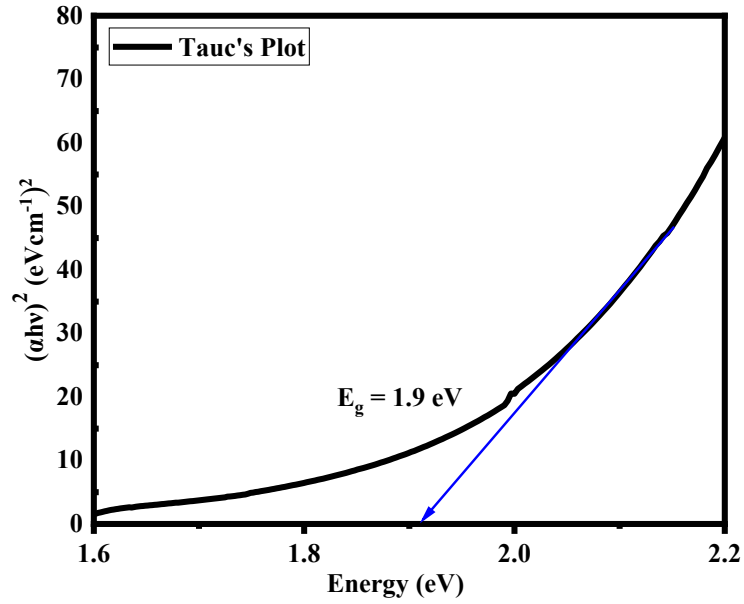
Figure 4.4 Tauc's plot for Perovskite

The literature has extensively shown that MAFAPbI$_3$ has a narrower bandgap (1.48 ≈1.50 eV) than MAPbI3. Consequently, the band gap can be adjusted by mixing FA$^+$ with them to generate the mix-cation FA$_{0.4}$MA$_{0.6}$PbI$_3$ (Gao et al., 2020). The bandgap of FA$_{0.4}$MA$_{0.6}$PbI$_3$ perovskite using Tauc's method was 1.9 (eV) (Figure 4.4) which means it absorbs photons with a slightly higher energy compared to perovskites with a smaller band gap.

4.4   Photoluminescence (PL) Spectroscopy

The PL (photoluminescence) analysis was carried out using a spectrofluorometer (model- FS5) to study the emission intensity of any material. Moreover, this technique provides insights into the recombination processes of

charge carriers occurring in the material. The excitation wavelength was set to be at 350 nm. The excitation wavelength of 350 nm corresponds to the energy required to excite electrons from the ground state to higher energy states in many organic luminescent materials (Kabe and Adachi, 2017).
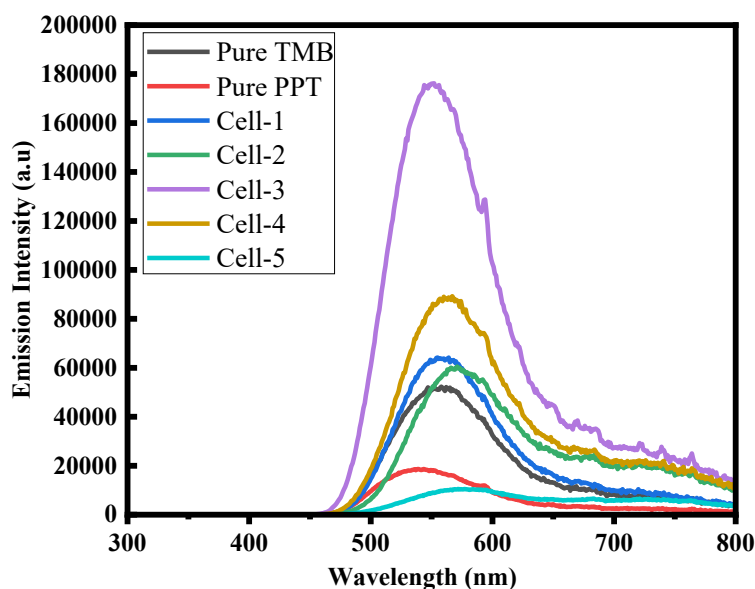
Figure 4.5 PL spectra of OLPL with various ratio of TMB and PPT

Analyzing the unique PL characteristics of the TMB-PPT combination is crucial because these characteristics, such as emission intensities and wavelengths, may be affected by a number of variables, including the surrounding environment, the concentrations of TMB and PPT, and the interactions between the two materials. The electronic transitions occurring in PPT and TMB when combined and stimulated at 350 nm resulted in clearly visible PL spectra. Organic Compound TMB, is well renowned for its robust electron-donating capabilities. The molecule

can efficiently transfer charges due to its structure (Figure 4.6(a)), which facilitates the effective charge transport inside the substance. TMB absorbs photons at 350 nm and prompts electrons within its molecules to transition to higher energy levels. In the presence of light, these excited electrons can release energy upon recombination.
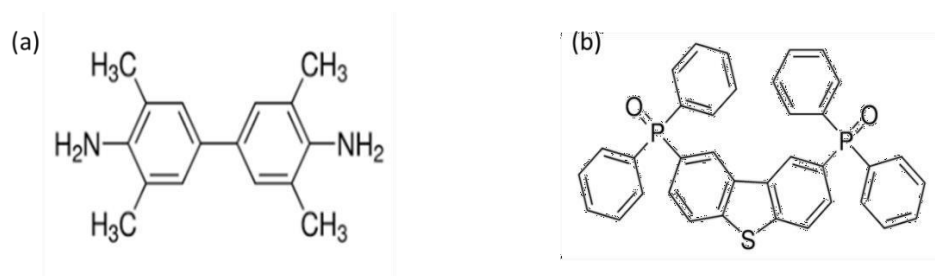
Figure 4.6 Structure of (a) TMB (b) PPT (Dong et al., 2021)

In the same way, PPT experiences electronic changes upon photon absorption at 350 nm. The Excitation of electrons can lead to their holes resulting in the emission of light (Nishimura et al., 2020). Consequently, the resultant spectra of cell-1 to cell-5, pure TMB, and pure PPT show maximum peaks that correspond to the emission from TMB and PPT between 530 and 570 nm, except for cell-2 as shown in Figure 4.5. The strong electron-donating qualities of TMB are responsible for its superior PL emission in pure form when compared to PPT. Small amounts of TMB radical cations, which should be absorbed in longer wavelength regions, maybe the cause of this prolonged absorption.
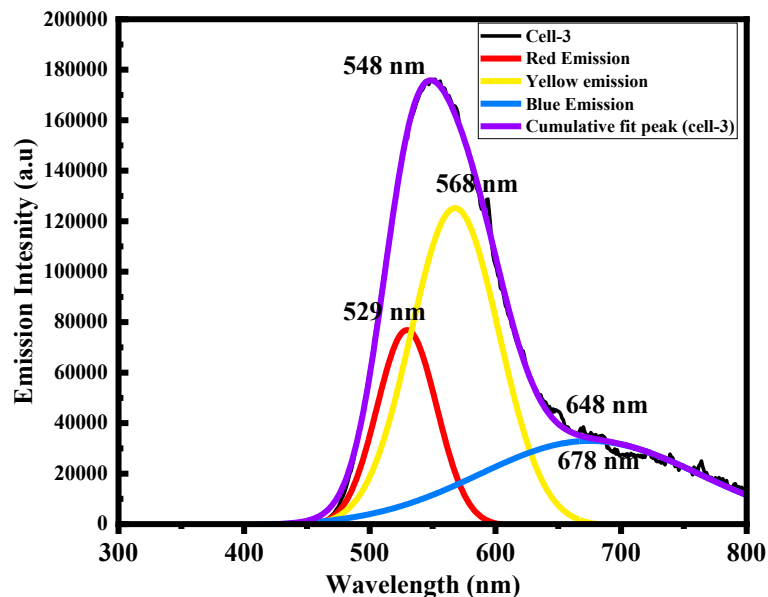
Figure 4.7 Deconvolution of the photoluminescence for cell-3

For a better understanding of this behavior, Gaussian fitting with replicas, of which the three Gaussian adjustments simulating each luminescence spectrum in the cumulative curve were applied. The deconvolution spectra from the optimized sample (cell-3) with their respective adjustments are shown insight of Figure 4.7. There was a significant rise in PPT concentration. At the same time, there has been evidence of red, yellow, and blue emission, and the emission spectra have slightly changed from 548 nm to 568 nm.

4.5   Time-resolved photoluminescence (TRPL) spectroscopy

The photon count and lifespan of the organic luminescent compounds were determined using TRPL spectroscopy. A decay curve was produced as a function of time by recording the emission of the material over time using a pulsed laser as

the excitation source. The lifetime (τ) of charge carriers can be determined by using the exponential decay function of the photoluminescence intensity:

Short Lifetime: Short lifetime shows that charge carriers are recombining quickly, which may be the result of material flaws or non-radiative recombination processes.

Long Lifetime: A long lifetime indicates that an electron in the excited state stays there for a longer period, resulting in slower recombination between the charge carriers. Generally, a slower recombination rate indicates fewer defects. Optoelectronic devices, such as SCs, tend to have longer lifetimes because their efficiency improves as their lifetime increases.

Decay of Photon Count: The lifetime of the excited state is found by measuring the rate at which the photon count drops with time. If more than one process is present, the decay may frequently be fitted with one or more exponential functions to extract distinct recombination durations (Chuliá-Jordán and Juarez-Perez, 2022)

In this work, the emission decay dynamics of OLPL material were investigated using TRPL spectroscopy. After PPT and TMB were blended, TRPL spectra were recorded, which are crucial for comprehending the recombination and carrier dynamics inside the material. The lifespan and photon count of each sample are shown in Figure 4.8. Based on the findings, every sample shows nearly the same pattern. Among the luminescence blend samples, cell-3 exhibits the highest photon counts and longest lifespan, suggesting the slowest rate of electron decay. When compared to the pure PPT sample, Cell-3's lifetime analysis reveals a longer

lifetime. As a result, among the blend luminescence samples, the rate of photon emission has accelerated from cell 3, indicating the material's concentration of radiative recombination centers and radiative recombination efficiency (Xing et al., 2017). With the exception of cell-1 and cell-2, all of the cells had extended carrier lifetimes because of the rise in recombination rates brought upon by blended luminescence's trap states.
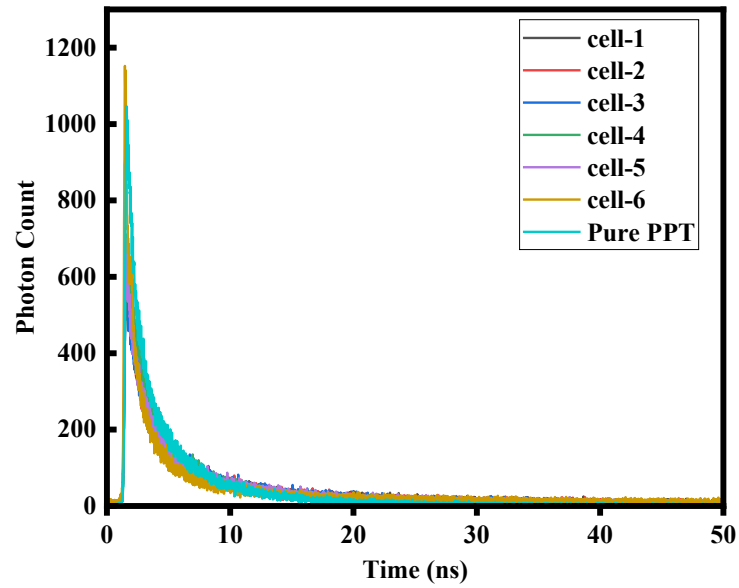
Figure 4.8 TRPL spectra of LPL (TMB-PPT)

Using the following triple-exponential equation, the samples' lifespan data were evaluated:

$$R(t) = B_1 e^{(-t/\tau 1)} + B_2 e^{(-t/\tau 2)} + B_3 e^{(-t/\tau 3)} \qquad (4.3)$$

Here B1, B2 and B3 represents the amplitude constituent of the first, second and third decay exponents, respectively. The decay curve is made up of two slower

50

components, τ2 and τ3, and one quick component, τ1. Pure PPT has an average luminous lifetime of 4.226 ns.
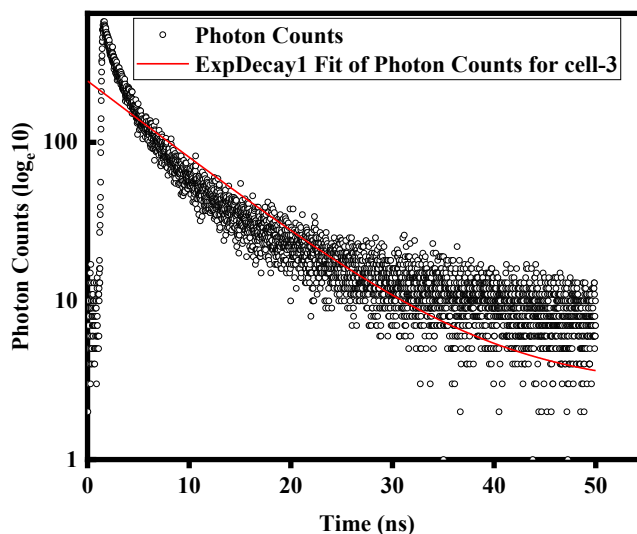
Figure 4.9 Fitting of TRPL of LPL (cell-3)

As in the cases of cell-1 and cell-2, where a larger ratio of PPT to TMB is blended, the corresponding lifespan values are 2.133 ns and 2.110 ns. With 7.197 ns, Cell-3 has the longest lifespan value (τ1 = 0.674 ns, τ2 = 2.527 ns, τ3 = 9.997 ns). Longer lifespans appear to be sustained by a higher ratio of TMB in the mix blend, as seen by cells 4 and 5, which had lifetime values of 6.020 and 6.592 ns. Since the observed lifespan is short, which is at 7 ns, OLPL blends are expected to have short-lived or negligible luminescence effects, which conflicts with the properties of LPL materials. However, as Table 4.1 demonstrates, all of the cells, with the exception of cells 1 and 2, had extended carrier lifetimes because of a rise in recombination rates brought on by the trap states found in LPL blend.

Remarkably, this investigation did not examine the impact of excitation power. Additionally, the samples' applicability was only verified at room temperature.

Table 4.1. Charge Lifetime extracted from the TRPL spectra of LPL

	T1	T2	T3	B1	B2	B3	T1^2	T2^2	T3^2	Life time τ (ns)
Pure PPT	0.313	2.279	6.795	0.007	0.002	0.001	0.098	5.194	46.174	4.226
Cell-1	0.615	2.506	10.686	0.002	0.002	0	0.378	6.280	114.197	2.133
Cell-2	0.487	2.435	10.531	0.002	0.002	0	0.237	5.929	110.906	2.110
Cell-3	0.674	2.526	9.996	0.001	0.002	0.001	0.454	6.385	99.932	7.196
Cell-4	0.390	2.227	8.518	0.002	0.002	0.001	0.152	4.961	72.568	6.019
Cell-5	0.344	2.172	9.883	0.002	0.002	0.001	0.118	4.719	97.675	6.592

4.6 XRD (X-Ray Diffraction) of LPL

XRD technique was used to analyze the specific phase of the LPL layer and to recognize whether the prepared material is compatible with the existing perovskite structure. Figure 4.10 depicts the XRD patterns of the blended LPL (TMB-PPT) of ratio (7:3) as well as individual LPL in its pure state. The strong broad diffraction pattern of the pure PPT (Figure 4.10a) compound, centered at 16.97°, suggests that the PPT compound lacks the crystal lattice and that the molecular or atomic arrangements are more disorientated whereas the pure TMB and the mixture of blended TMB-PPT have fully crystalline nature (Figure 4.10 b & c) which shows two peaks at 13.10° and 23.43°. The crystalline phase of blended LPL affects in longer lifetime of charges, allows for a higher chance of charge extraction, and contributes to higher device efficiencies which is further verified by I-V characteristics.
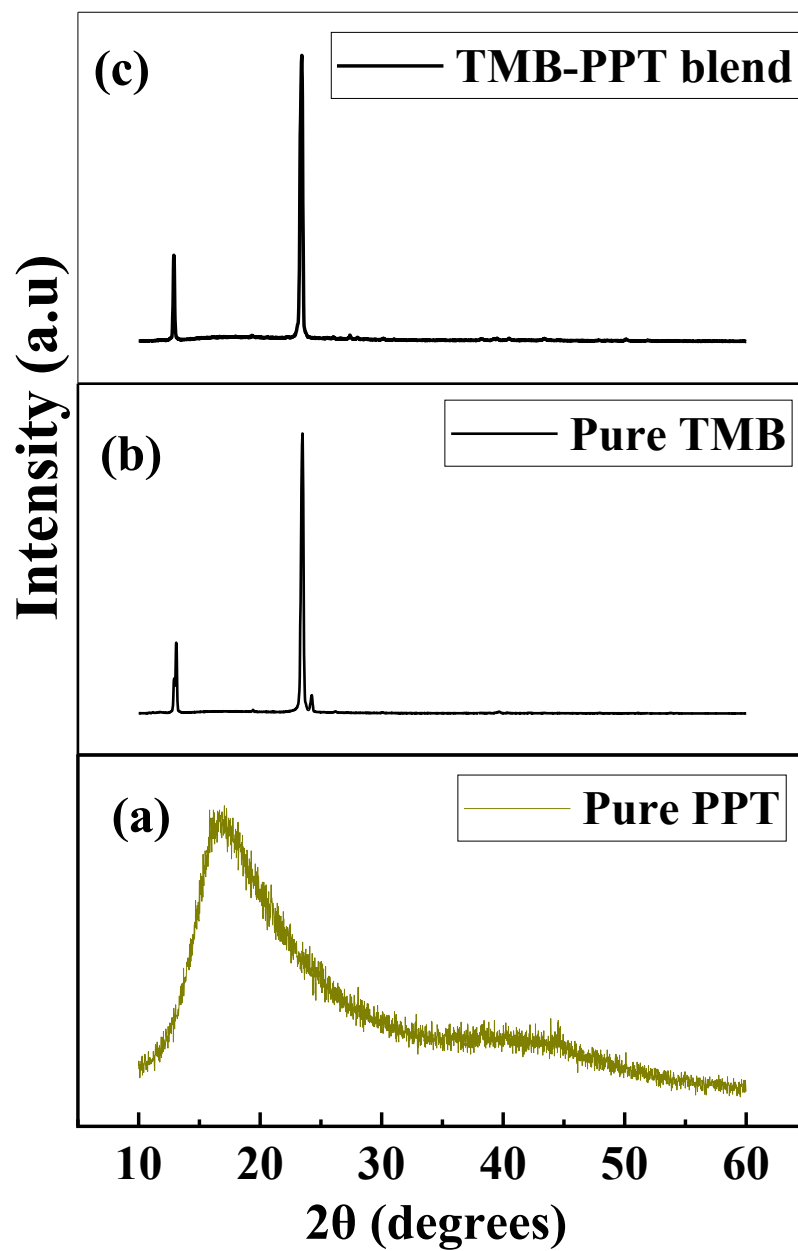
Figure 4.10 XRD pattern of (a) Pure PPT (b) Pure TMB (c) blend TMB-PPT (7:3)

4.7   XRD of Perovskite

To determine the crystal structure and phase purity of the perovskites, XRD analysis was employed. In addition to providing information about the lattice structure, this technique ensures that the synthesized material will have the desired crystalline phase, which is necessary for high-efficiency SCs. Therefore, Figure 4.11 shows the XRD pattern of $FA_{0.4}MA_{0.6}PbI_3$ perovskite film and the matching JCPDS: 01-0731752. The peak observed in the JCPDS database corresponds to PbI_2. The database did not include any peaks that corresponded to methylammonium lead iodide or formamidinium iodide. Peaks corresponding to formamidinium iodide and methylammonium lead iodide were not identified in the database. The lattice planes that correspond to the diffraction peaks for 2θ values of 14.06°, 26.54°, and 28.26° are (003), (013), and (014), respectively. In the perovskite film, the diffraction peak at 14.06° exhibits a preferred orientation with a higher intensity, where 0.4 M of FA is incorporated into the $MA_{0.6}PbI_3$ perovskite film causing the diffraction intensity to become much stronger, suggesting higher crystallinity which causes the expanding the lattice parameters of $FA_{0.4}MA_{0.6}PbI_3$. Since FA ions are larger than MA ions, the lattice size is increased with FA incorporation, according to Bragg's equation ($2d \sin\theta = n\lambda$) (Maqsood et al., 2020). This was evident that perovskites have a tetragonal structure in their crystal structure, as confirmed by these peaks.
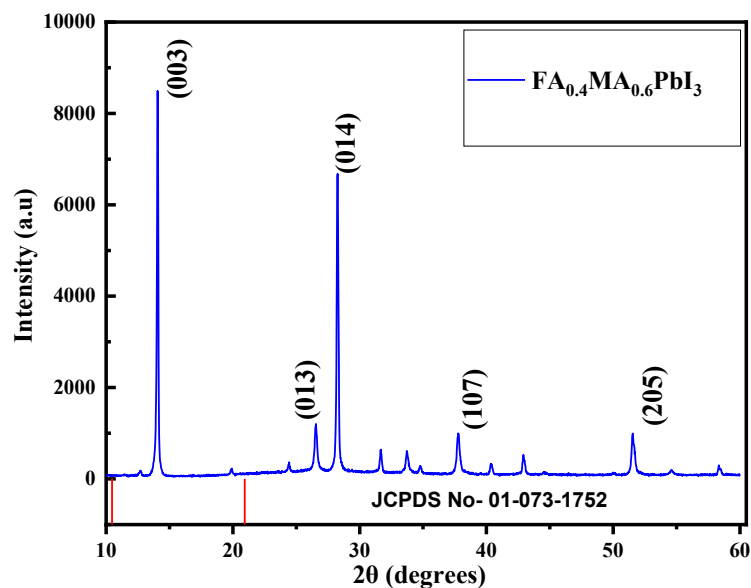
Figure 4.11 XRD pattern of Perovskite $FA_{0.4}MA_{0.6}PbI_3$

4.8   SEM (Scanning electron microscopy)

The surface morphology and microstructure of the perovskite films were examined using SEM. SEM offers high-resolution pictures that show the surface roughness, size, and pinholes. The performance of the SCs is directly affected by both the uniformity and the identification of defects in the perovskite layer, which may be achieved with the use of this characterization technique. The perovskite films of $FA_{0.4}MA_{0.6}PbI_3$ are seen in the top-view of SEM as shown in Figure 4.12. The size of perovskite particle was found to be significantly altered by the ratio of FA^+. Figure 4.12(a) shows the clear formation of perovskite with proper uniform crystal packing, and no pinhole has been found. Furthermore, compared to $MAPbI_3$, which has already been extensively studied in the literature, the $FA_{0.4}MA_{0.6}PbI_3$ perovskite film shows

better cubic particle form and a more distinct grain boundary (Chen et al., 2018). As the FA^+ ratio rises, the $FA_{0.4}MA_{0.6}PbI_3$ perovskite film's size increases. The $FAPbI_3$ perovskite film has the biggest grains among the $FA_{0.4}MA_{0.6}PbI_3$ perovskite films specifically when the MA^+ is replaced by the FA^+ ion. This is because the FA^+ gives the $FA_{0.4}MA_{0.6}PbI_3$ perovskite film a more compacted surface and greater grain size. On the other hand, Figure 4.12(b) was an image obtained from the coated sample with inadequate coverage whereas the $FA_{0.4}MA_{0.6}PbI_3$ perovskite film is observed to have a uniform crystal layer. This results in a more compact surface and bigger grain size because the FA^+ contribution in the $FA_{0.4}MA_{0.6}PbI_3$ perovskite film is somewhat higher (Yang et al., 2019).
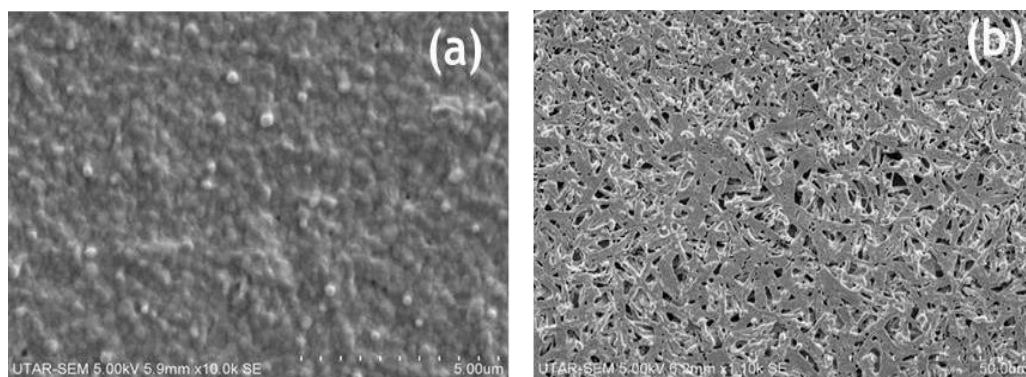
Figure 4.12 SEM of Perovskite at magnification (a) 10 μm (b) 50 μm

4.9 Field Emission Scanning Electron Microscopy (FESEM) Analysis

The detailed surface investigation was conducted using FESEM, which has a greater resolution than normal SEM in which a tungsten filament is used as an electron source. The size of pinholes and grain boundaries inside the perovskite films may be better understood by using FESEM, which makes it possible to observe finer morphological details and nano-scale characteristics. Unlike SEM, a field emission electron source is used in FESEM. This source usually consists of a field emitter or a sharp metal tip that enables the creation of electrons through a process called field emission. In both cases, Figure 4.13 (a) and (b) respectively there is structure composed of large grains. The homogeneous, pinhole-free perovskite film shown in Figure 4.13 (a) and (b) was obtained by incorporating FA cations into pristine MAPbI$_3$ (FA$_{0.4}$MA$_{0.6}$PbI$_3$) (Maqsood et al., 2020). A grain size of 0.226 μm is associated with its closely packed structure. In contrast, Figure 4.13 (c) and (d) demonstrate the presence of pinholes with the average size of 0.712 μm in the perovskite film, together with several grain boundaries, which promotes nonradiative recombination and reduces the PSCs' efficiency. Due to this large size of pinholes, the uniformity of the perovskite layer has been significantly through charge extraction. High pinhole density can lead to non-uniform light absorption or emission across the device area (Zhu et al., 2021). This occurrence of pinholes is due to the prolonged exposure of the perovskite samples to the open environment over an extended period. Consequently, a gradual degradation of the samples has been observed. It is noteworthy that the perovskite samples reported in this work were

not subjected to any form of encapsulation (Tafazoli et al., 2018; Wang et al., 2017).
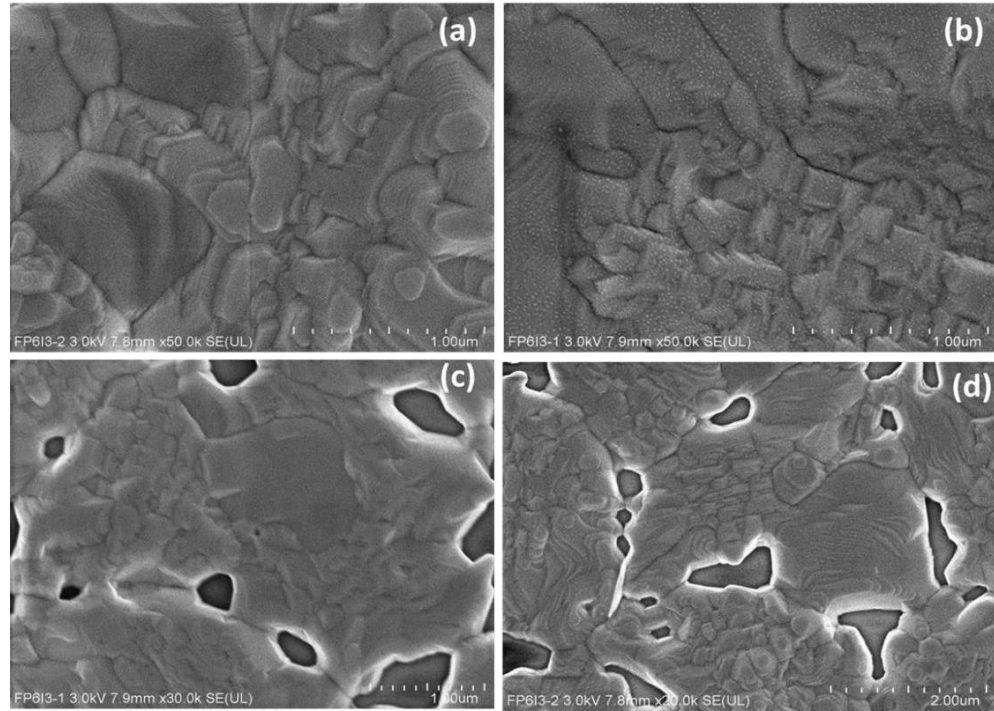
Figure 4.13 FESEM images of top view of Perovskite

4.10 High-Resolution Transmission Electron Microscopy (HRTEM) Analysis

Unlike SEM or FESEM, HRTEM provides unique insights into the characteristics of the material. With the use of HRTEM, imaging at the atomic scale is made possible, yielding comprehensive details on atomic configurations, lattice structures, and crystal structural defects. Through electron diffraction patterns, HRTEM also offers comprehensive crystallographic information that enables the identification of various phases and fringe distances. This information includes the

59

shape and composition of various layers and their interfaces.

Therefore, Figures 4.14(a) and (b) depict the original FAMAPbI$_3$ in its crystalline phase, which displays a tetragonal crystal structure, before degradation. The HRTEM images of a FAMAPbI$_3$ film (Figure 4.10 (a), inset of Figure 4.14 (a)) show interplanar distances of 0.18 nm, which is corresponding to the (211) plane of the cubic perovskite structure. In contrast, the addition of FA$^+$ (0.4 M of FA$^+$ / 0.6 M of MA$^+$) results in the creation of 5-100 nm-sized nanoscopic spherical 3D crystals as depicted in Figure 4.13(c) and (d). The alternation affects the morphology of the perovskite, consequently of FA$^+$ / 0.6 M of MA$^+$), consequently impacting the performance of PSCs. The perovskite crystal influences various photovoltaic parameters, such as charge carrier mobility, recombination losses, and stability. These factors contribute to enhanced power conversion efficiencies (PCEs) in mixed cation PSC devices, making them favorable for I-V analysis (Lee et al., 2012; Pathak et al., 2015).
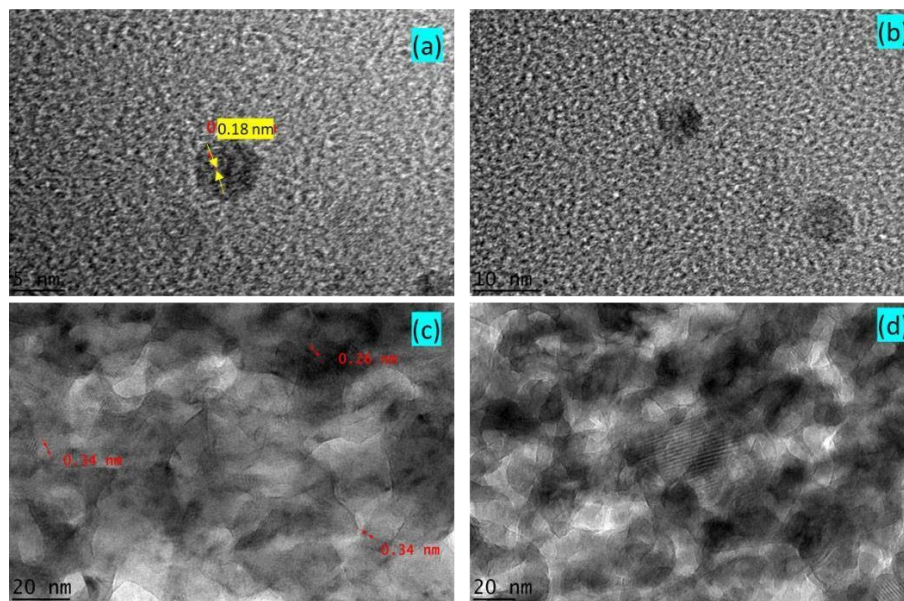
Figure 4.14 HRTEM of Perovskite

4.11 Photovoltaic parameters of PSCs (J-V) curve

The performance of PSCs was determined through J-V analysis under standardized test (STG) conditions using a solar simulator. The PSC's active area in this experiment was 0.16 cm^2. The measurements were made with an illumination condition of 0.73 suns, or 7.3 mW/cm². By keeping this parameter, consistent and reproducible testing can be achieved, allowing for the accurate measurement of PCE, short-circuit current (J_{sc}), open-circuit voltage (V_{oc}), and fill factor (FF).
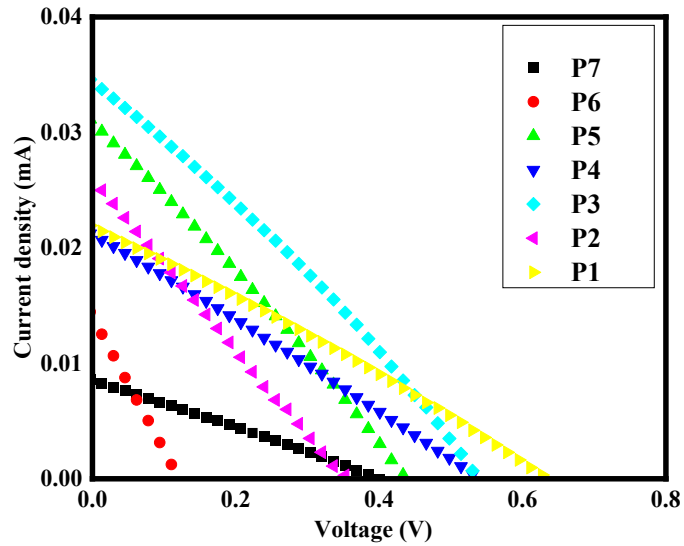
Figure 4.15 J-V curve of PSCs coupled with OLPL/ILPL measured with solar simulator under xenon lamp

The PSC devices are fabricated using three distinct materials each having their photocurrent density−voltage properties are displayed in Table 4.2 and Figure 4.15. The findings showed that certain individual materials had a major impact on the overall power conversation efficiency (PCE). The P6 device with OLPL has the lowest photovoltaic performance, with a (V_{oc}) of 0.221 V, a (FF) of 24.80, a (J_{sc}) of 25.05 mA/cm^2, and a PCE of 1.06%. This shows that OLPL has a negligible impact on the device. This observation is consistent with the TRPL analysis's short charge lifetime (section 4.5). Charge recombination that happens quickly when photoexcited in the OLPL layer may be the cause of poor self-illumination upon light soaking. Additionally, the effect of using polyvinyl alcohol (PVA) as an HTL, deposited as a thin layer over the perovskite layer, followed by a carbon electrode,

has been examined. Unfortunately, the outcome reveals the device (P7) has the second lowest performance, with a (V_{oc}) of 0.370 V, a (FF) of 24.80, a (J_{sc}) of 8.36 mA/cm^2, and a PCE of 1.20%. This poor performance is caused by the high internal resistance at the contact between the polymer electrolyte PVA and the perovskite (Rahul et al., 2016). In contrast, the device P3 with ILPL (based on strontium) shows a champion efficiency of 7.65%, with a (V_{oc}) of 0.537 V, a (FF) of 28.97, a (J_{sc}) of 34.40 mA/cm^2. Even though the assembly with the OLPL layer performed poorly in the dark, there is still an opportunity for development since better LPL layer encapsulation might result in longer charge lifetimes and longer periods of self-illumination.

Table 4.2 Photovoltaic measurement of PSC samples with OLPL and ILPL, with polymer electrolyte

S.No	Composition	Voc (V)	Jsc (mA.cm^{-2})	FF	η (%)
P1	$FA_{0.4}MA_{0.6}PbI_3$	0.461± 0.08	31.83± 5.72	27.45± 2.80	5.76± 0.04
P2	$FA_{0.4}MA_{0.6}PbI_3$	0.355± 0.03	27.38± 1.12	24.63± 0.26	3.25± 0.65
P3	ILPL- $FA_{0.4}MA_{0.6}PbI_3$	0.537± 0.01	34.40± 0.20	28.97± 0.13	7.65± 0.20
P4	$FA_{0.4}MA_{0.6}PbI_3$	0.550± 0.02	21.77± 0.40	26.53± 1.37	4.12± 0.52
P5	$FA_{0.4}MA_{0.6}PbI_3$	0.437± 0.12	12.44± 1.07	27.03± 0.74	2.20± 0.10
pP6	OLPL- $FA_{0.4}MA_{0.6}PbI_3$	0.221± 0.07	25.05± 0.07	24.80± 0.52	1.06± 0.47
P7	$FA_{0.4}MA_{0.6}PbI_3$ _PVA	0.370± 0.02	8.36+ 0.09	26.24+ 0.34	1.20+ 0.01

4.12   Stability Study

PSCs may experience several degradation processes over time that lower their performance and efficiency. Therefore, to study the lifetime and reliability of PSCs, stability testing is crucial. These measurements have been performed under the same STG condition as described in section 4.15. Moisture is the primary factor

contributing to the degradation of PSC, hence device stability under ambient environment is crucial for the development of PSCs. The carbon layer has the ability to function as a barrier, preventing water molecules from entering into the perovskite layer. This investigation examined the stability of the device made in room ambient conditions without any encapsulation. The devices underwent weekly testing for a total duration of 1800 hours. The detailed characteristics for all fabricated devices are shown in Figure 4.16. The devices fabricated without using polymer electrolyte show a significantly slower rate of degradation than those fabricated using polymer electrolyte. This might be because the interfaces inside the SC are more stable in the absence of PVA, allowing the various PSCs layers to function together more effectively and without breaking down (Wang et al., 2018). Throughout the duration of the test, the device experienced an 89.9% decrease in its power conversion efficiency (PCE) from the initial point to the end. During the period between 500 to 800 hours, the PCE consistently maintained a stable trend, fluctuating between 5.01% and 5.50%. This observed stability can be attributed to the photo-chemical stability even after exposure to light. Additionally, the whole device fabrication and testing of PSCs have been performed at room-temperature which indicates good thermal stability. The highly hydrophobic nature of carbon indicating a robust performance during this period. However, a notable deviation in the trend occurred at 1176 hours, marked by a sudden drop in PCE to 3.31%. Despite this decline, the PCE resumed a constant trend from 1176 to 1512 hours, once again demonstrating the chemically stable and highly hydrophobic nature of carbon as a contributing factor to the observed behavior.
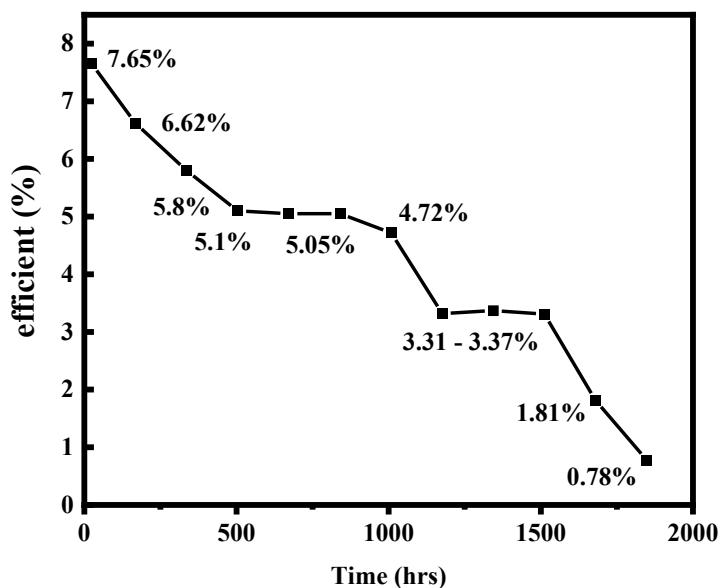
Figure 4.16 Stability measurements of device exposed in ambient atmosphere without encapsulation tested under xenon lamp illumination

4.13   Electrochemical Impedance Spectroscopy (EIS)

In order to comprehend the interfacial charge-transfer characteristics at the interface between the charge transport layer and the perovskite film, EIS was utilized to examine the dynamic response of PSC samples. Figure 4.17 - 4.19 displays the Nyquist plots that were obtained with a light source where two samples were analyzed namely: ILPL-based PSC, and PSC with OLPL at a bias voltage of 0.6 V, the frequency range was scanned from 100 Hz to 10 Hz. The selected frequency range covers a broad variety of dynamic processes. Therefore, high frequencies (100 Hz) can explore quick processes like charge transfer resistance and capacitance at

the interfaces, at the same time lower frequencies (10 Hz) can offer information on slower processes like ion migration and recombination (Lazanas and Prodromidis, 2023). The inset within all the graphs illustrates the equivalent electronic circuit for the carbon-perovskite interface. Figure 4.17 - 4.19 shows the simulated and experimental Nyquist plot results of OLPL-based PVSC, ILPL-based PVSC, and planar PSCs to study the kinetic behavior of the devices. The EIS spectra for all devices concerning their configuration were measured experimentally as well as with simulation. The simulated results and experimental data agreed well with their respective configuration of the device. A useful aspect of simulating EIS spectra is that it is possible to predict parameters like series resistance (R_s) and polarization resistance (R_p) by extra plotting the experimental data. The measurements were then fitted with an equivalent circuit consisting of two parallel combinations of resistors and capacitors (C1‖R2) and (C2‖R3) as indicated by Figure 4.18 and Figure 4.19.
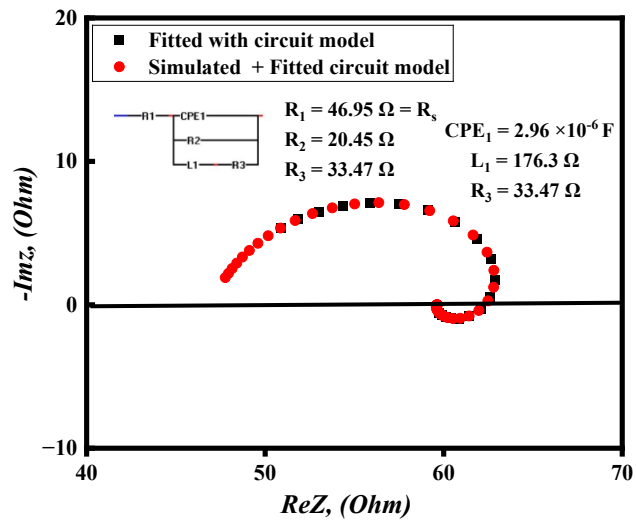
Figure 4.17 Nyquist plot of PSC with OLPL

Figure 4.17 shows the obvious high-frequency semicircle ranging from 46 to 64 Ω is revealing the polarization resistance as the effect of coupling between the perovskite and OLPL. It has a large high-frequency arc, which is explained by the recombination resistance and geometric capacitance. The series resistance (R_s) serves as the starting point for the Nyquist plot's real part (ReZr). The individual circuit values and their corresponding series and charge transfer resistance values are shown in Table 4.3. The series resistance of the PSC incorporating OLPL material registers at 47 Ω. It is immediately evident that there are inductive loops, constant phase elements (CPE1), and arcs of intermediate frequency with negative impedance. It is possible that the dynamic nature of perovskites can contribute to negative impedance, as they can exhibit ion migration and polarization effects (Calado et al., 2016 ; Moia et al., 2023).
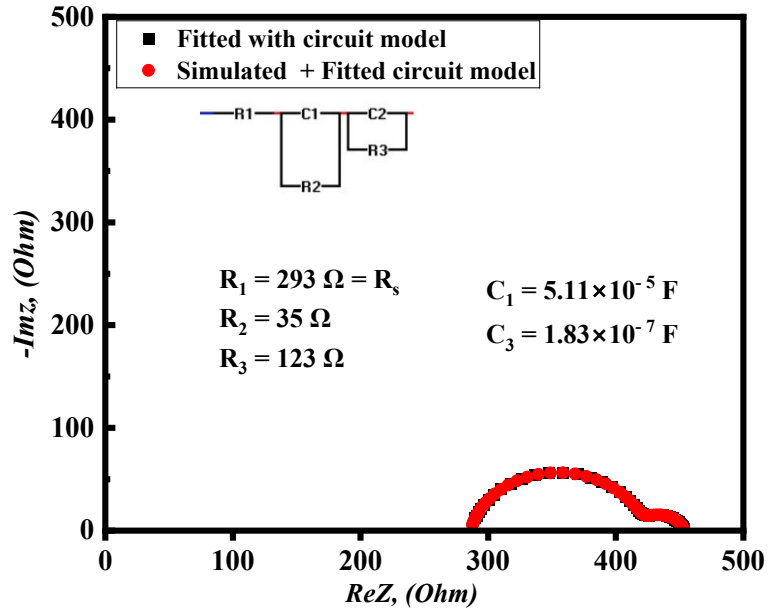
Figure 4.18 Nyquist plot of PSC with ILPL

Figure 4.18 portrays a high-frequency semicircle ranging from 0 to 500 Ω revealing the polarization resistance (R_p) as the effect of coupling between the perovskite and ILPL with a series resistance 290 Ω.
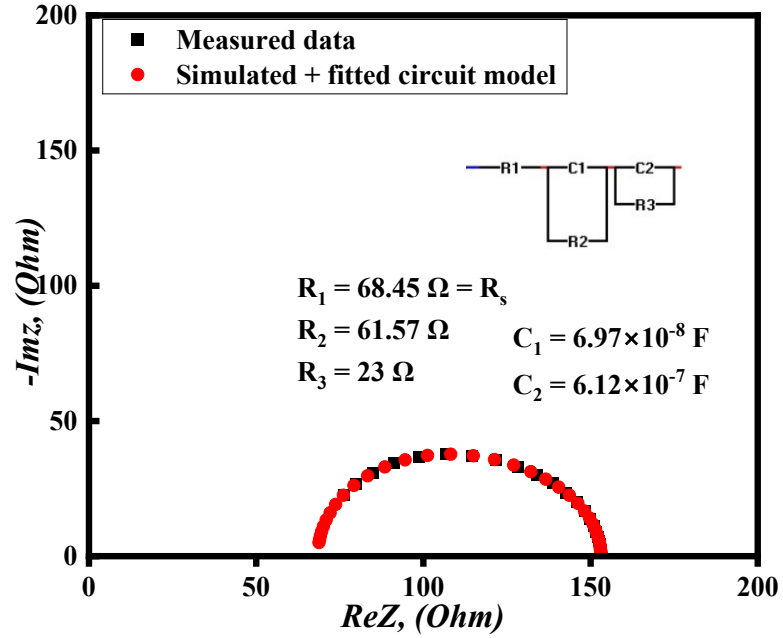
Figure 4.19 Nyquist plot of Planar PSC

Similarly, Figure 4.19 displays the Nyquist plot fitted equivalent circuit for PVSC having a configuration as $FTO/c\text{-}TiO_2/m\text{-}TiO_2/Perovskite/carbon$, respectively. Based on the relatively series resistance of 68.45 Ω, appears to have very few shunting paths, which is advantageous for reducing leakage currents and enhancing overall device efficiency (Breitenstein et al., 2008). At the same time, the calculated (R_p) value of 153 Ω indicates the resistance to charge flow within the device (Hauff and Klotz, 2022 ; Kirui et al., 2021). Additionally, it was observed that

carbon-based PVSC exhibits a higher Voc as that compared to other cells. This higher Voc value suggests that carbon films could function as efficient passivation layers, lowering charge carrier recombination at interfaces or inside the perovskite layer (Almora et al., 2024).

Table 4.3 EIS Relevant Circuit values for C-PSCs

Device	CPE	C_1 (F)	C_2 (F)	Rp (Ω)	$R_S=R_1$ (Ω)	R_2 (Ω)	R_3 (Ω)	Charge lifetime (sec)
OLPL-PSC	2.96×10^{-6}	1.33×10^{-5}	0	59	46.95	20.45	33.47	2.71×10^{-4}
ILPL-PSC	0	5.11×10^{-5}	1.83×10^{-7}	453	293	35	123	1.78×10^{-3}
Planar PSC	0	6.94×10^{-8}	6.12×10^{-7}	153	68.45	61.57	23	3.76×10^{-6}

As described in Table 4.3, the widely-known characteristic, electron lifetime or charge lifetime as shown in Table 2, determines the average amount of time an electron stays in the material's conduction band before recombining with a hole or being removed as photocurrent. In the case of OLPL-based PSC, the relatively short electron lifetime ($\tau = 2.71\times10^{-4}$ sec) suggests a higher rate of electron-hole recombination. Additionally, the equivalent circuit shows in Figure 4.17 consisting of constant phase element (CPE) which is used to model imperfect capacitive behavior of electrical system. Therefore, equivalent capacitance of a CPE in a parallel R-CPE circuit has been calculated by the equation 4.4.

$$C = R^{(1-\alpha/\alpha)}. Q^{1/\alpha} \tag{4.4}$$

Where R is the resistance associated parallelly with the CPE, α is number of CPEs,

Q is the numerical value of CPE. In general, organic materials exhibit modest charge carrier mobilities and may experience reduced charge lifetimes due to trap-mediated recombination. Even though it is externally connected, the OLPL can influence the charge mobility in the PSC (Morab et al., 2023). Thus, the (τ = 2.71×10^{-4} sec) measured charge duration implies that the OLPL affects the kinetics of charge transport and recombination, leading to a shorter charge lifetime (Wen et al., 2016). This is also likely to be the cause of the low efficiency (1.06%) of PSC based on OLPL. In comparison to the OLPL, the ILPL, which is also externally coupled with PSC, offers superior charge transport characteristics. It also has fewer trap states. The calculated charge lifetime of (τ = 1.78×10^{-3} sec) shows that, in comparison to the OLPL, the ILPL considerably extends the charge lifetime by enhancing charge transport and lowering recombination rates inside the PSC structure. On the other hand, in the absence of any externally coupled LPL, the value of (τ = 3.76 ×10^{-6} sec) indicates a substantially reduced charge lifetime. A substantially reduced charge lifetime and fast charge carrier recombination might result from ineffective charge extraction in the absence of an LPL (Hsieh et al., 2020).

CHAPTER-5

CONCLUSIONS AND RECOMMENDATIONS

5.1 Conclusion

In conclusion, analysis of the emission decay rate of blended organic long persistent luminescence (LPL) materials shows similar pattern for photon counts with blended LPL cells. In the mixed luminescence blend samples, cell-3 = 7:3) displays the highest photon counts and longest lifetime, indicating the lowest rate of electron decay. Thus, cell-3 emits more photons than the mix luminescence blend samples, demonstrating better recombination effectiveness in the material. This indicates that cell-3 is more efficient at recombination, which can improve the SC's total efficiency by reducing energy losses from non-radiative processes. This increase in recombination efficacy raises the possibility of higher efficiencies for PSCs with LPL materials that are optimized. In order to enhance photon emission and reduce electron decay, future development efforts can concentrate on optimizing the ratios of LPL materials, which will result in SCs with higher efficiency. The performances of C-PSC with blended OLPL and ILPL materials have been successfully assessed. The fabricated PSC device was stable up to 1680 hours. Compared to the control sample, the device with OLPL shows a decrement in efficiency of 1.75 %. Although there is a huge drop in efficiency, this result implies that more optimization on the luminescent layer is required. This decrease in device efficiency is ascribed to the luminescence layer's light-blocking and light-

absorbing properties, which lower the quantity of photons that can reach the perovskite layer.

Furthermore, this work also compares the PCE of PSC with polymer electrolyte. The PCE of the PSC structure FTO/TiO$_2$/Perovskite/C was found to be 5.76 %. The samples underwent a thorough analysis that included UV-VIS, XRD, SEM, and TRPL. Additionally, there is no discernible increase in power conversion for PSCs coupled with OLPL, comparative to ILPL which achieved the champion efficiency of 7.65%. Due to this significant difference in band gaps between the perovskite layer and the LPL material (> 2.0 eV), the PCE of the PSC is significantly affected. The photovoltaic performance of PSCs confirms that this may result in charge transfer issues, hindering the efficient extraction of photogenerated carriers from the additional material to the perovskite layer. It is not completely ruled out that the structure of the SC might be partially shorted. For this reason, optimization of configuration is necessary. The findings demonstrated that PSC fabricated under room ambient conditions and its performance can be improved by employing different techniques, such as HTL-free structure and VASP technique. Lastly, the band gap of the perovskite may be efficiently controlled by combining different ion species. According to the shown stability, PSCs' lifetime may be greatly increased by including luminescent material. As a result, PSCs may become more prepared for the market which may draw investment and commercial interest. Moreover, PSCs with optimized luminescence materials have the potential to achieve great efficiency and stability, making them formidable competitors in the solar industry. More work is needed to improve the transport properties of the absorber

layer and the carbon/perovskite interface to lower the devices' series resistance.

According to the EIS measurement, the observed charge duration of (τ = 2.71×10^{-4} sec) suggests that the OLPL influences the charge transport and recombination kinetics, resulting in a reduced charge lifetime. Based on OLPL, this is also probably the reason behind PSC's low efficiency (1.06%). Moreover, the externally coupled LPLs may not behave as direct passivation layers for the perovskite material, but they can still affect charge lifetime by influencing charge transport characteristics inside the SC structure. With a charge lifetime of 1.78×10^{-3} seconds, the ILPL outperforms the OLPL in terms of charge transport and lowers recombination rates inside the structure of the PSC resulting in a substantially longer charge lifetime and a higher PCE. Conversely, in the case when there is no externally connected LPL, the value of (τ = 3.76×10^{-6} sec) denotes a significantly shorter charge lifetime. Ineffective charge extraction in the absence of an LPL may lead to a much shorter charge lifetime and rapid charge carrier recombination.

Improvements in PSC technology have the potential to greatly increase SC's efficiency, especially when luminescent materials are used. Higher efficiency makes solar energy more competitive with conventional energy sources since more electricity can be produced from the same amount of sunlight. In addition, the lifetime of PSCs can be increased by enhancing their stability by the use of luminescent materials. This results in lower maintenance costs and increases the long-term durability of solar power panels by reducing the need for regular replacements. PSC developments also help to progress material science and make

it possible to develop lightweight SCs that may be used for a range of purposes, including building-integrated photovoltaics and portable electronics. Its commercialization and large-scale manufacturing can boost employment and economic growth, particularly in areas that make significant infrastructure investments in renewable energy.

5.2   Future Recommendation

It is crucial to note that problems like material compatibility, integration techniques, and long-term performance validation require continuing study. The area is dynamic, and further developments might be made in the future to improve PSCs stability, which is essential to their widespread use. Improved encapsulation techniques and the development of advanced barrier layers can effectively shield perovskite materials from external factors such as moisture and oxygen. Optimizing the interfaces between polymer electrolyte and the perovskite, ETL and perovskite/HTL, can mitigate the degradation pathways. Luminescent layers can be incorporated into tandem designs to enhance light management, optimize energy transfer between layers, and contribute to the overall stability of the device. In order to enhance photon emission and reduce electron decay, future development efforts can concentrate on optimizing the ratios of LPL materials, which will result in SCs with higher efficiency. Polymers like polyvinylpyrrolidone (PVP), poly (methyl methacrylate) (PMMA) and polyvinylidene fluoride (PVDF) should be explored as additives or coatings to stabilize the perovskite layer, which can improve the resistance of perovskite films to moisture, enhance crystallinity, and reduce defects,

leading to enhanced stability and reduced degradation over time. Future studies should concentrate on balancing stability and efficiency by optimizing the concentration and composition of luminescence materials. Investigating various organic luminescence materials and their blends can lead to breakthroughs in the pursuit of increased efficiency.

REFERENCES

Quanyao Lin, Dominik J. Kubicki, MirKazem Omrani, Firoz Alam, Mojtaba Abdi-Jalebi (2023). 'The race between complicated multiple cation/anion compositions and stabilization of FAPbI₃ for halide perovskite solar cells', 11(7). Available at: https://doi.org/10.1039/d2tc04529j.

Acik, M., & Darling, S. B. (2016). Graphene in perovskite solar cells: device design, characterization and implementation. *J. Mater. Chem. A*, *4*(17), 6185–6235. https://doi.org/10.1039/C5TA09911K

Alam, P., Cheung, T. S., Leung, N. L. C., Zhang, J., Guo, J., Du, L., Kwok, R. T. K., Lam, J. W. Y., Zeng, Z., Phillips, D. L., Sung, H. H. Y., Williams, I. D., & Tang, B. Z. (2022). Organic Long-Persistent Luminescence from a Single-Component Aggregate. *Journal of the American Chemical Society*, *144*(7), 3050–3062. https://doi.org/10.1021/jacs.1c11480

Assi, A., Rashid Saleh, W., & Mohajerani, E. (2021). Effect of Metals (Au, Ag, and Ni) as Cathode Electrode on Perovskite Solar Cells. *IOP Conference Series Earth and Environmental Science*, *722*. https://doi.org/10.1088/1755-1315/722/1/012019

Azmi, R., Hadmojo, W. T., Sinaga, S., Lee, C.-L., Yoon, S. C., Jung, I. H., & Jang, S.-Y. (2018). High-Efficiency Low-Temperature ZnO Based Perovskite Solar Cells Based on Highly Polar, Nonwetting Self-Assembled Molecular Layers. *Advanced Energy Materials*, *8*(5), 1701683. https://doi.org/https://doi.org/10.1002/aenm.201701683

Azmi, R., Hwang, S., Yin, W., Kim, T.-W., Ahn, T. K., & Jang, S.-Y. (2018). High

efficiency low-temperature processed perovskite solar cells integrated with alkali metal doped. *ACS Energy Letters*, *3*(6), 1241–1246. https://doi.org/10.1021/acsenergylett.8b00493

Babu, V., Fuentes Pineda, R., Ahmad, T., Alvarez, A. O., Castriotta, L. A., Di Carlo, A., Fabregat-Santiago, F., & Wojciechowski, K. (2020). Improved Stability of Inverted and Flexible Perovskite Solar Cells with Carbon Electrode. *ACS Applied Energy Materials*, *3*(6), 5126–5134. https://doi.org/10.1021/acsaem.0c00702

Best Research-Cell Efficiencies. (2020). 2020.

Bett, A. J., Schulze, P. S. C., Winkler, K. M., Kabakli, Ö. S., Ketterer, I., Mundt, L. E., Reichmuth, S. K., Siefer, G., Cojocaru, L., Tutsch, L., Bivour, M., Hermle, M., Glunz, S. W., & Goldschmidt, J. C. (2020). Two-terminal Perovskite silicontandem solar cells with a high-Bandgap Perovskite absorber enabling voltages over 1.8 V. *Progress in Photovoltaics: Research and Applications*, *28*(2), 99–110. https://doi.org/https://doi.org/10.1002/pip.3208

Caprioglio, P., Zu, F., Wolff, C. M., Márquez Prieto, J. A., Stolterfoht, M., Becker, P., Koch, N., Unold, T., Rech, B., Albrecht, S., & Neher, D. (2019). High open circuit voltages in pin-type perovskite solar cells through strontium addition. *Sustainable Energy and Fuels*, *3*(2), 550–563. https://doi.org/10.1039/c8se00509e

Chen, H., & Yang, S. (2019). Methods and strategies for achieving high-performance carbon-based perovskite solar cells without hole transport materials. *J. Mater. Chem. A*, *7*(26), 15476–15490. https://doi.org/10.1039/C9TA04707G

Chen, L. C., Lee, K. L., Wu, W. T., Hsu, C. F., Tseng, Z. L., Sun, X. H., & Kao, Y. T. (2018). Effect of Different $CH_3NH_3PbI_3$ Morphologies on Photovoltaic Properties of Perovskite Solar Cells. *Nanoscale Research Letters*, *13*. https://doi.org/10.1186/s11671-018-2556-8

Chen, L., Cao, H., Wang, S., Luo, Y., Tao, T., Sun, J., & Zhang, M. (2019). Efficient air-stable perovskite solar cells with a $(FAI)_{0.46}(MAI)_{0.40}(MABr)_{0.14}(PbI_2)_{0.86}(PbBr_2)_{0.14}$ active layer fabricated: Via a vacuum flash-assisted method under RH > 50%. *RSC Advances*, *9*(18), 10148–10154. https://doi.org/10.1039/c9ra01625b

Chen, X., Xia, Y., Huang, Q., Li, Z., Mei, A., Hu, Y., Wang, T., Cheacharoen, R., Rong, Y., & Han, H. (2021). Tailoring the Dimensionality of Hybrid Perovskites in Mesoporous Carbon Electrodes for Type-II Band Alignment and Enhanced Performance of Printable Hole-Conductor-Free Perovskite Solar Cells. *Advanced Energy Materials*, *11*(18), 2100292. https://doi.org/https://doi.org/10.1002/aenm.202100292

Chiatti, C., Fabiani, C., & Pisello, A. L. (2021). *Long Persistent Luminescence: A Road Map Toward Promising Future Developments in Energy and Environmental Science*. 51:409-433 https://doi.org/10.1146/annurev-matsci-091520-011838

Chuliá-Jordán, R. and Juarez-Perez, E.J. (2022) 'Short Photoluminescence Lifetimes Linked to Crystallite Dimensions, Connectivity, and Perovskite Crystal Phases', Journal of Physical Chemistry C, 126(7), pp. 3466–3474. Available at: https://doi.org/10.1021/acs.jpcc.1c08867.

Dehingia, A., Das, U., & Roy, A. (2022). Partial replacement of B-site cation to stabilize

the optically active cubic phase of FAPbI$_3$ for optoelectronic applications. *Materials Today: Proceedings*, *65*, 29–34. https://doi.org/https://doi.org/10.1016/j.matpr.2022.04.031

Den Eeckhout, K. Van, Smet, P. F., & Poelman, D. (2010). Persistent Luminescence in Eu^{2+}-Doped Compounds: A Review. *Materials*, *3*, 2536–2566. https://api.semanticscholar.org/CorpusID:5123234

Deng, Y., Lu, S., Xu, Z., Zhang, J., Ma, F., & Peng, S. (2020). Enhanced performance of CdS/CdSe quantum dot-sensitized solar cells by long-persistence phosphors structural layer. *Science China Materials*, *63*(4), 516–523. https://doi.org/10.1007/s40843-019-1248-6

Di Giacomo, F., Zardetto, V., D'Epifanio, A., Pescetelli, S., Matteocci, F., Razza, S., Di Carlo, A., Licoccia, S., Kessels, W. M. M., Creatore, M., & Brown, T. M. (2015). Flexible Perovskite Photovoltaic Modules and Solar Cells Based on Atomic Layer Deposited Compact Layers and UV-Irradiated TiO2 Scaffolds on PlasticSubstrates. *Advanced Energy Materials*, *5*(8), 1401808. https://doi.org/https://doi.org/10.1002/aenm.201401808

Dong, Q., Shi, Y., Wang, K., Li, Y., Wang, S., Zhang, H., Xing, Y., Du, Y., Bai, X., & Ma, T. (2015). Insight into Perovskite Solar Cells Based on SnO$_2$ Compact Electron-Selective Layer. *The Journal of Physical Chemistry C*, *119*(19), 10212–10217. https://doi.org/10.1021/acs.jpcc.5b00541

Dong, H. et al. (2021) 'Organic composite materials: Understanding and manipulating

excited states toward higher light-emitting performance', Aggregate, 2. Available at: https://doi.org/10.1002/agt2.103.

Doki, N., Maruyama, K. and Yokota, M. (2024) 'Formation and Properties of Organic Long Persistent Luminescence Crystals Containing Benzidine Derivatives by Melt Crystallization', Advances in Chemical Engineering and Science, 14(01), pp. 1–7. Available at: https://doi.org/10.4236/aces.2024.141001.

Du, J., Qiu, C., Li, S., Zhang, W., Zhang, W., Wang, Y., Qiu, Z., Wang, Q., Yang, K., Mei, A., Rong, Y., Hu, Y., & Han, H. (2022). Minimizing the Voltage Loss in Hole-Conductor-Free Printable Mesoscopic Perovskite Solar Cells. *Advanced Energy Materials*, *12*(1), 2102229. https://doi.org/https://doi.org/10.1002/aenm.202102229

Duan, J., Xu, H., Sha, W. E. I., Zhao, Y., Wang, Y., Yang, X., & Tang, Q. (2019). Inorganic perovskite solar cells: An emerging member of the photovoltaic community. *Journal of Materials Chemistry A*, *7*(37), 21036–21068. https://doi.org/10.1039/c9ta06674h

Duan, J. et al. (2018) 'Planar perovskite $FA_xMA_{1-x}PbI_3$ solar cell by two-step deposition method in air ambient', Optical Materials, 85(August), pp. 55–60. Available at: https://doi.org/10.1016/j.optmat.2018.07.072.

Etacheri, V., Di Valentin, C., Schneider, J., Bahnemann, D., & Pillai, S. C. (2015). Visible-light activation of TiO_2 photocatalysts: Advances in theory and experiments. *Journal of Photochemistry and Photobiology C: Photochemistry Reviews*, *25*, 1–29. https://doi.org/https://doi.org/10.1016/j.jphotochemrev.2015.08.003

Gao, L. K., Tang, Y. L., & Diao, X. F. (2020). Theoretical study on photoelectric properties of FAPbI3 doped with Ge. *Materials Research Express*, *7*(11). https://doi.org/10.1088/2053-1591/ab9edf

Habisreutinger, S. N., & Blackburn, J. L. (2021). Carbon nanotubes in high-performance perovskite photovoltaics and other emerging optoelectronic applications. *Journal of Applied Physics*, *129*(1), 10903. https://doi.org/10.1063/5.0035864

Haghighi, M. et al. (2023) 'Low-Temperature Processing Methods for Tin Oxide as Electron Transporting Layer in Scalable Perovskite Solar Cells', Solar RRL, 7(10), p. 2201080. Available at: https://doi.org/https://doi.org/10.1002/solr.202201080.

Hoang Huy, V. P., & Bark, C.-W. (2023). Review on Surface Modification of SnO_2 Electron Transport Layer for High-Efficiency Perovskite Solar Cells. *Applied Sciences*, *13*(19). https://doi.org/10.3390/app131910715

Huang, S. et al. (2021) 'Efficiency improvement of solar cells by $CaAlSiN_3{:}Eu^{2+}$ and $Y_2O_3{:}Eu^{3+}$ phosphors', Journal of Physics: Conference Series, 2065(1). Available at: https://doi.org/10.1088/1742-6596/2065/1/012005.

Huang, W. et al. (2021) 'Room Temperature Processed Double Electron Transport Layers for Efficient Perovskite Solar Cells', pp. 2–11. https://doi.org/10.3390/nano11020329

Im, J.-H., Jang, I.-H., Pellet, N., Grätzel, M., & Park, N.-G. (2014). Growth of CH3NH3PbI3 cuboids with controlled size for high-efficiency perovskite solar cells. *Nature Nanotechnology*, *9*(11), 927–932. https://doi.org/10.1038/nnano.2014.181

Joseph J.D, Jasmin M., J., & Sidharth., R.S (2022). Fabrication and characterization of silicon solar cells towards improvement of power efficiency. *Materials Today: Proceedings*,*62*,2050–2055.

https://doi.org/https://doi.org/10.1016/j.matpr.2022.02.493

Jeong, S. and Lee, J. (2011) 'Dibenzothiophene derivatives as host materials for high efficiency in deep blue phosphorescent organic light emitting diodes', J. Mater. Chem., 21, pp. 14604–14609. Available at: https://doi.org/10.1039/C1JM12421H.

Ji, F., Wang, L., Pang, S., Gao, P., Xu, H., Xie, G., Zhang, J., & Cui, G. (2016). A balanced cation exchange reaction toward highly uniform and pure phase $FA_{1-x}MA_xPbI_3$ perovskite films. *Journal of Materials Chemistry A*, *4*, 14437–14443. https://doi.org/10.1039/c6ta05727f

Kabe, R. and Adachi, C. (2017b) 'Organic long persistent luminescence', Nature, 550 (7676), pp. 384–387. Available at: https://doi.org/10.1038/nature24010.

Kavan, L., Tétreault, N., Moehl, T., & Grätzel, M. (2014). Electrochemical Characterization of TiO$_2$ Blocking Layers for Dye-Sensitized Solar Cells. *The Journal of Physical Chemistry C*, *118*(30), 16408–16418. https://doi.org/10.1021/jp4103614

Ke, W., Fang, G., Liu, Q., Xiong, L., Qin, P., Tao, H., Wang, J., Lei, H., Li, B., Wan, J., Yang, G., & Yan, Y. (2015). Low-temperature solution-processed tin oxide as an alternative electron transporting layer for efficient perovskite solar cells. *Journal of the American Chemical Society*, *137*(21), 6730–6733. https://doi.org/10.1021/jacs.5b01994

Kim, M., Kim, G., Oh, kyoung suk, Jo, Y., Yoon, H., Kim, K.-H., Lee, H., Kim, J. Y., & Kim, D. (2017). A High Temperature-Short Time Annealing Process for High Performance Large-Area Perovskite Solar Cells. *ACS Nano*, *11*. https://doi.org/10.1021/acsnano.7b02015

Kumar Soni, A., & Pratap Singh, B. (2020). Luminescent Materials in Lighting, Display, Solar Cell, Sensing, and Biomedical Applications. *Luminescence - OLED Technology and Applications*, 1–23. https://doi.org/10.5772/intechopen.82123

Lee, A. Y., Park, D. Y., & Jeong, M. S. (2018). Correlational study of halogen tuning effect in hybrid perovskite single crystals with Raman scattering, X-ray diffraction, and absorption spectroscopy. *Journal of Alloys and Compounds*, *738*, 239–245. https://doi.org/https://doi.org/10.1016/j.jallcom.2017.12.149

Lee, M. M., Teuscher, J., Miyasaka, T., Murakami, T. N., & Snaith, H. J. (2012). Efficient hybrid solar cells based on meso-superstructured organometal halide perovskites. *Science (New York, N.Y.)*, *338*(6107), 643–647.

https://doi.org/10.1126/science.1228604

Li, P., Hua, Y., Ye, R., Cai, M., Xu, S., & Zhang, J. (2022). $SrAl_2O_4$ crystallite embedded inorganic medium with super-long persistent luminescence, thermoluminescence, and photostimulable luminescence for smart optical information storage. *Photon. Res.*, *10*(2), 381–388. https://doi.org/10.1364/PRJ.444145

Li, T. et al. (2020) 'Anatase TiO_2 nanorod arrays as high-performance electron transport layers for perovskite solar cells', Journal of Alloys and Compounds, 849, p. 156629. Available at: https://doi.org/https://doi.org/10.1016/j.jallcom.2020.156629.

Li, X., Bi, D., Yi, C., Décoppet, J.-D., Luo, J., Zakeeruddin, S. M., Hagfeldt, A., & Grätzel, M. (2016). A vacuum flash–assisted solution process for high-efficiency large-area perovskite solar cells. *Science*, *353*(6294), 58–62. https://doi.org/10.1126/science.aaf8060

Li, Y., Gecevicius, M., & Qiu, J. (2016). Long persistent phosphors - From fundamentals to applications. *Chemical Society Reviews*, *45*(8), 2090–2136. https://doi.org/10.1039/c5cs00582e

Li, Z., Kulkarni, S. A., Boix, P. P., Shi, E., Cao, A., Fu, K., Sudip, K., Zhang, J., Xiong, Q., Wong, L. H., Mathews, N., & Mhaisalkar, S. G. (2014). *Laminated Carbon Nanotube Networks for Metal Electrode-Free Efficient Perovskite Solar Cells*. 8(7): 6797-804 https://doi.org/10.1021/nn501096h

Liu, N., Chen, X., Sun, X., Sun, X., & Shi, J. (2021). Persistent luminescence nanoparticles for cancer theranostics application. *Journal of Nanobiotechnology*,

19(1), 113. https://doi.org/10.1186/s12951-021-00862-z

Malevu, T. D., Mwankemwa, B. S., Motloung, S. V, Tshabalala, K. G., & Ocaya, R. O. (2019). Effect of annealing temperature on nano-crystalline TiO_2 for solar cell applications. *Physica E: Low-Dimensional Systems and Nanostructures*, *106*, 127–132. https://doi.org/https://doi.org/10.1016/j.physe.2018.10.028

Maqsood, A., Li, Y., Meng, J., Song, D., Qiao, B., Zhao, S., & Xu, Z. (2020). Perovskite Solar Cells Based on Compact, Exceeding 22 %. *Nanoscale Research Letters*, *15*(89), 1–9. http://dx.doi.org/10.1186/s11671-020-03313-0

Matsuzawa, T., Aoki, Y., Takeuchi, N., & Murayama, Y. (1996). vacumm. *Journal of The Electrochemical Society*, *143*(8), 2670. https://doi.org/10.1149/1.1837067

Nazeeruddin, M. K. (2016). In retrospect: Twenty-five years of low-cost solar cells. *Nature*, *538*(7626), 463–464. https://doi.org/10.1038/538463a

Nishimura, N., Lin, Z., Jinnai, K., Kabe, R., & Adachi, C. (2020). Many Exciplex Systems Exhibit Organic Long-Persistent Luminescence. *Advanced Functional Materials*, *30*(22), 1–6. https://doi.org/10.1002/adfm.202000795

Osobajo, O. A., Otitoju, A., Otitoju, M. A., & Oke, A. (2020). The Impact of Energy Consumption and Economic Growth on Carbon Dioxide Emissions. *Sustainability*, *12*(19). https://doi.org/10.3390/su12197965

Parashar, M., & Kaul, A. B. (2021). Methylammonium Lead Tri-Iodide Perovskite Solar Cells with Varying Equimolar Concentrations of Perovskite Precursors. *Applied Sciences*, *11*(24). https://doi.org/10.3390/app112411689

Pathak, S., Sakai, N., Wisnivesky Rocca Rivarola, F., Stranks, S. D., Liu, J., Eperon, G.

E., Ducati, C., Wojciechowski, K., Griffiths, J. T., Haghighirad, A. A., Pellaroque, A., Friend, R. H., & Snaith, H. J. (2015). Perovskite Crystals for Tunable White Light Emission. *Chemistry of Materials*, *27*(23), 8066–8075. https://doi.org/10.1021/acs.chemmater.5b03769

Pospisil, J., Shekargoftar, M., Hvojnik, M., Gemeiner, P., Weiter, M., & Dzik, P. (2020). *Perovskite Solar Cells with Low-Cost TiO₂ Mesoporous Photoanodes Prepared by Rapid Low-Temperature (70°C) Plasma Processing.* https://doi.org/10.1021/acsaem.0c02144

Pradid, P., Sanglee, K., Thongprong, N., & Chuangchote, S. (2021). Carbon Electrodes in Perovskite Photovoltaics. *Materials (Basel, Switzerland)*, *14*(20). https://doi.org/10.3390/ma14205989

Qiao, W.-C., Liang, J.-Q., Dong, W., Ma, K., Wang, X. L., & Yao, Y.-F. (2022). Formamidinium lead triiodide perovskites with improved structural stabilities and photovoltaic properties obtained by ultratrace dimethylamine substitution. *NPG Asia Materials*, *14*(1), 49. https://doi.org/10.1038/s41427-022-00395-3

Qin, J., Zhang, Z., Shi, W., Liu, Y., Gao, H., & Mao, Y. (2017). The optimum titanium precursor of fabricating TiO₂ compact layer for perovskite solar cells. *Nanoscale Research Letters*, *12*(1). https://doi.org/10.1186/s11671-017-2418-9

Qiu, C., Wu, Y., Song, J., Wang, W., & Li, Z. (2022). Efficient Planar Perovskite Solar Cells with ZnO Electron Transport Layer. *Coatings*, *12*(12). https://doi.org/10.3390/coatings12121981

Rahul, Bhattacharya, B., Singh, P. K., Singh, R., & Khan, Z. H. (2016). Perovskite sensitized solar cell using solid polymer electrolyte. *International Journal of*

Hydrogen Energy, *41*(4), 2847–2852. https://doi.org/https://doi.org/10.1016/j.ijhydene.2015.12.093

Riaz, S., & Park, S.-J. (2022). O, S-g-C$_3$N$_4$ nanotubes as photovoltaic boosters in quantum dot-sensitized all-weather solar cells: a synergistic approach for enhanced power conversion efficiency in dark-light conditions. *Materials Today Chemistry*, *26*, 101125. https://doi.org/https://doi.org/10.1016/j.mtchem.2022.101125

Saliba, M., Matsui, T., Domanski, K., Seo, J.-Y., Ummadisingu, A., Zakeeruddin, S., Correa-Baena, J.-P., Tress, W., Abate, A., Hagfeldt, A., & Graetzel, M. (2016). Incorporation of rubidium cations into perovskite solar cells improves photovoltaic performance. *Science (New York, N.Y.)*, *354*. https://doi.org/10.1126/science.aah5557

Saliba, M., Matsui, T., Seo, J.-Y., Domanski, K., Correa-Baena, J.-P., Nazeeruddin, M., Zakeeruddin, S., Tress, W., Abate, A., Hagfeldt, A., & Gratzel, M. (2016). Cesium-containing Triple Cation Perovskite Solar Cells: Improved Stability, Reproducibility and High Efficiency. *Energy & Environmental Science*. https://doi.org/10.1039/C5EE03874J

Salim, K. M. M., Masi, S., Gualdrón-Reyes, A. F., Sánchez, R. S., Barea, E. M., Krecmarová, M., Sánchez-Royo, J. F., & Mora-Seró, I. (2021). Boosting Long-Term Stability of Pure Formamidinium Perovskite Solar Cells by Ambient Air Additive Assisted Fabrication. *ACS Energy Letters*, *6*(10), 3511–3521. https://doi.org/10.1021/acsenergylett.1c01311

Shahiduzzaman, M. et al. (2020) 'Graphite/Carbon Black Counter Electrode Deposition Methods to Improve the Efficiency and Stability of Hole-Transport-Layer-Free

Perovskite Solar Cells', Nanomaterials (Basel, Switzerland), 10(9). Available at:
https://doi.org/10.3390/nano10091676.

Shanker, V., Haranath, D., & Swati, G. (2015). Persistence Mechanisms and
Applications of Long Afterglow Phosphors. *Defect and Diffusion Forum*, *361*, 69–
94. http://dx.doi.org/10.4028/www.scientific.net/DDF.361.69

Sibiński, M. (2023) 'Review of Luminescence - Based Light Spectrum Modifications
Methods and Materials for Photovoltaics Applications', Materials, 16(8). Available at:
https://doi.org/10.3390/ma16083112.

Snaith, H. J. (2013). Perovskites: The Emergence of a New Era for Low-Cost, High-
Efficiency Solar Cells. *The Journal of Physical Chemistry Letters*, *4*(21), 3623–
3630. https://doi.org/10.1021/jz4020162

Suresh Kumar, N., & Chandra Babu Naidu, K. (2021). A review on perovskite solar cells
(PSCs), materials and applications. *Journal of Materiomics*, *7*(5), 940–956.
https://doi.org/https://doi.org/10.1016/j.jmat.2021.04.002

Tafazoli, S., Timasi, N., Nouri, E., & Mohammadi, M. R. (2018). The role of a vapor-
assisted solution process on tailoring the chemical composition and morphology of
mixed-halide perovskite solar cells. *CrystEngComm*, *20*(31), 4428–4435.
https://doi.org/10.1039/c8ce00628h

Tang, H., He, S., & Peng, C. (2017). A Short Progress Report on High-Efficiency
Perovskite Solar Cells. *Nanoscale Research Letters*, *12*(1), 410.
https://doi.org/10.1186/s11671-017-2187-5

Tang, H., Xu, T., Qin, X., Zou, K., Lv, S., Fan, J., Huang, T., Chen, L., & Huang, W. (2021). Carbon Quantum Dot-Passivated Perovskite/Carbon Electrodes for Stable Solar Cells. *ACS Applied Nano Materials*, *4*(12), 13339–13351. https://doi.org/10.1021/acsanm.1c02850

Teixeira, C. O., Castro, D., Andrade, L., & Mendes, A. (2022). Selection of the ultimate perovskite solar cell materials and fabrication processes towards its industrialization: A review. *Energy Science \& Engineering*, *10*(4), 1478–1525. https://doi.org/https://doi.org/10.1002/ese3.1084

Triana, S.L., Kusumandari and Suryana, R. (2016) 'Effect of wet etching process on the morphology and transmittance of fluorine doped tin oxide (FTO)', Journal of Physics: Conference Series, 776(1). Available at: https://doi.org/10.1088/1742-6596/776/1/012005.

Uddin, A., & Yi, H. (2022). Progress and Challenges of SnO2 Electron Transport Layer for Perovskite Solar Cells: A Critical Review. *Solar RRL*, *6*(6), 2100983. https://doi.org/https://doi.org/10.1002/solr.202100983

Vaidyanathan, S. (2023). Recent progress on lanthanide-based long persistent phosphors: an overview. *J. Mater. Chem. C*, *11*(26), 8649–8687. https://doi.org/10.1039/D2TC05243A

Wang, D., Zhang, L., Deng, K., Zhang, W., Song, J., Wu, J., & Lan, Z. (2018). Influence of Polymer Additives on the Efficiency and Stability of Ambient-Air Solution-Processed Planar Perovskite Solar Cells. *Energy Technology*, *6*(12), 2380–2386. https://doi.org/https://doi.org/10.1002/ente.201800378

Wang, J. F., Zhu, L., Zhao, B. G., Zhao, Y. L., Song, J., Gu, X. Q., & Qiang, Y. H. (2017). Surface engineering of perovskite films for efficient solar cells. *Scientific Reports*, *7*(1), 1–9. https://doi.org/10.1038/s41598-017-14920-w

Wang, X. et al. (2014) 'Influence of compact TiO$_2$ layer on the photovoltaic characteristics of the organometal halide perovskite-based solar cells', Materials Science in Semiconductor Processing, 27, pp. 569–576. Available at: https://doi.org/10.1016/j.mssp.2014.07.039.

Wu, T., Ono, L., Yoshioka, R., Ding, C., Zhang, C., Mariotti, S., Zhang, J., Mitrofanov, K., Liu, X., Segawa, H., Kabe, R., Han, L., & Qi, Y. (2022). Elimination of light-induced degradation at the nickel oxide-perovskite heterojunction by aprotic sulfonium layers towards long-term operationally stable inverted perovskite solar cells. *Energy & Environmental Science*, *15*. https://doi.org/10.1039/D2EE01801B

Xing, Y., Wang, L., Yang, D., Wang, Z., Hao, Z., Sun, C., & Xiong, B. (2017). A novel model on time-resolved photoluminescence measurements of polar InGaN / GaN multi- quantum-well structures. *Nature Publishing Group*, *October 2016*, 1–9. https://doi.org/10.1038/srep45082

Xu, S., Chen, R., Zheng, C., & Huang, W. (2016). Excited State Modulation for Organic Afterglow: Materials and Applications. *Advanced Materials*, *28*(45), 9920–9940. https://doi.org/10.1002/adma.201602604

Xu, Y., Lin, Z., Wei, W., Hao, Y., Liu, S., Ouyang, J., & Chang, J. (2022). Recent Progress of Electrode Materials for Flexible Perovskite Solar Cells. *Nano-Micro Letters*, *14*(1), 117. https://doi.org/10.1007/s40820-022-00859-9

Xue, T., Chen, D., Li, T., Chou, X., Wang, X., Tang, Z., Zhang, F., Huang, J., Guo, K., & Takaloo, A. V. (2023). Boosting the Performance of Perovskite Solar Cells through Systematic Investigation of the Annealing Effect of E-Beam Evaporated TiO_2. *Micromachines*, *14*(6). https://doi.org/10.3390/mi14061095

Yan, N., Fang, Z., Dai, Z., Feng, J., & Liu, S. (Frank). (n.d.). Improved perovskite/carbon interface. *Advanced Functional Materials*, *n/a*(n/a), 2314039. https://doi.org/https://doi.org/10.1002/adfm.202314039

Yang, F., Dong, L., Jang, D., Saparov, B., Tam, K. C., Zhang, K., Li, N., Brabec, C. J., & Egelhaaf, H.-J. (2021). Low Temperature Processed Fully Printed Efficient Planar Structure Carbon Electrode Perovskite Solar Cells and Modules. *Advanced Energy Materials*, *11*(28), 2101219. https://doi.org/https://doi.org/10.1002/aenm.202101219

Yang, W. S., Park, B.-W., Jung, E. H., Jeon, N. J., Kim, Y. C., Lee, D. U., Shin, S. S., Seo, J., Kim, E. K., Noh, J. H., & Seok, S. Il. (2017). Iodide management in formamidinium-lead-halide-based perovskite layers for efficient solar cells. *Science (New York, N.Y.)*, *356*(6345), 1376–1379. https://doi.org/10.1126/science.aan2301

Yang, Y., Luo, J., Wei, A., Liu, J., Zhao, Y., & Xiao, Z. (2019). Study of perovskite solar cells based mixed-organic-cation $FA_xMA_{1-x}PbI_3$ absorption layer. *Physical Chemistry Chemical Physics*, *21*. https://doi.org/10.1039/C9CP02003A

Yi, C., Luo, J., Meloni, S., Boziki, A., Ashari-Astani, N., Grätzel, C. K., Zakeeruddin, S. M., Rothlisberger, U., & Grätzel, M. (2016). Entropic stabilization of mixed A-

cation ABX_3 metal halide perovskites for high performance perovskite solar cells. *Energy and Environmental Science*, *9*, 656–662. http://dx.doi.org/10.1039/C5EE03255E

Zhou, H. et al. (2014) 'Hole-Conductor-Free, Metal-Electrode-Free $TiO_2/CH_3NH_3PbI_3$ Heterojunction Solar Cells Based on a Low-Temperature Carbon Electrode', The Journal of Physical Chemistry Letters, 5(18), pp. 3241–3246. Available at: https://doi.org/10.1021/jz5017069.

Zeng, P., Deng, W., & Liu, M. (2020). Recent Advances of Device Components toward Efficient Flexible Perovskite Solar Cells. *Solar RRL*, *4*(3), 1900485. https://doi.org/https://doi.org/10.1002/solr.201900485

Zhang, L., Zhang, X., & Zhao, C. (2022). Crystal structure, luminescence properties and thermal stability of novel $Sr_2CaLa(VO_4)_3$: Sm^{3+} phosphor synthesized by the combustion method. Journal of Alloys and Compounds, *899*, 163378. https://doi.org/10.1016/j.jallcom.2021.163378

Zhang, T., Liu, C., Li, Z., Zhao, B., Bai, Y., Li, X., Liu, W., Chen, Y., Liu, Z., & Li, X. (2022). Improved Perovskite/Carbon Interface through Hot-Pressing: A Case Study for $CsPbBr_3$-Based Perovskite Solar Cells. *ACS Omega*, *7*(20), 16877– 16883. https://doi.org/10.1021/acsomega.1c06108

Zhao, Q., Wu, R., Zhang, Z., Xiong, J., He, Z., Fan, B., Dai, Z., Yang, B., Xue, X., & Cai, P. (2019). The mixing effect of organic cations on the structural, electronic and optical properties of $FA_xMA_{1-x}PbI_3$ perovskites. Organic Electronics, 71, 106– 112. https://doi.org/10.1039/C7CP06608B

Zhu, Y., Lai, G., Yi, J., Zhang, T., Zhang, Y., Wen, S., & Zhou, H. (2021). High-quality, Pb-free, pinhole-reduced $MA_{0.7}FA_{0.3}SnBr_3$ perovskite photodetector via incorporating graphite. Journal of Alloys and Compounds, *866*, 158990. https://doi.org/https://doi.org/10.1016/j.jallcom.2021.158990

LIST OF PUBLICATIONS

Sharma, T., Nguyen, T.T.H., Nguyen, N.H., Soo, Y.H., Ng, C.Y., & Jun, H.K*. (2024) 'Computational, optical and feasibility studies of organic luminescence TMB-PPT blend for photovoltaic application', Heliyon, 10(4), p. e26048. Available at: https://doi.org/10.1016/j.heliyon.2024.e26048.

Grishika Arora, Sharma, T., Foo Wah Low, Chai Yan Ng, Pramod K. Singh, Chiam-Wen Liew, Jun, H.K* (2024). 'Next-Generation Supercapacitors with Sustainably Processed Carbon Quantum Dots'. In book: Materials for Energy Conversion and Storage. Available at: http://dx.doi.org/10.1201/9781003314424-6

Sharma, T., Soo, Y.H., Ng, C.Y., Jun, H.K*. (2023) 'Effect of Organic Long Persistent Luminescence on Hole Transport Material-Free Perovskite Solar Cell', in 2023 International Conference on Power and Renewable Energy Engineering (PREE), pp. 27–31. Available at: https://doi.org/10.1109/PREE57903.2023.10370422.

Sharma, T. and Jun, H.K*. (2023) 'Characterization study of perovskite solar cells with incorporation of organic long persistent luminescence', in 2023 IEEE International Conference on Sensors and Nanotechnology (SENNANO), pp. 5–8. Available at: https://doi.org/10.1109/SENNANO57767.2023.10352525.

Ahmad, H., Sharma, T., Ng, C.Y., Jun, H.K*. (2023) 'Synthesis, characterization and electrochemical impedance study of CdS quantum dot-sensitized solar cell with reduced graphene oxide/TiO_2 composite photoanode', Bulletin of Materials Science, 46(1), p. 44. Available at: https://doi.org/10.1007/s12034-022-02878-z.

Abhimanyu Singh*, Pawan Singh Dhapola, Subhrajit Konwar, Sharma, T, H.K. Jun, Diksha Singh, Karol Strzałkowski, M.N. Masri, M.Z.A. Yahya, Markus Diantoro, Pramod K. Singh (2023) Ionic liquid (1-ethyl-3-methyltricynomethanide) doped polymer electrolyte (polyvinyl alcohol) for sustainable energy devices. Available at: https://doi.org/10.1016/j.jsamd.2023.100566